Received: 29 December 2018 | Revised: 10 September 2019 | Accepted: 30 November 2019

DOI: 10.1111/gbi.12376

ORIGINAL ARTICLE

gebiology WILEY

Microaerophilic Fe-oxidizing micro-organisms in Middle Jurassic ferruginous stromatolites and the paleoenvironmental context of their formation (Southern Carpathians, Romania)

Mihaela Grădinaru[1] | Iuliana Lazăr[1] | Mihai N. Ducea[1,2] | Lucian Petrescu[3]

[1]Department of Geology, Faculty of Geology and Geophysics, University of Bucharest, Bucharest, Romania

[2]Department of Geosciences, University of Arizona, Tucson, AZ, USA

[3]Department of Mineralogy, Faculty of Geology and Geophysics, University of Bucharest, Bucharest, Romania

Correspondence
Mihaela Grădinaru and Iuliana Lazăr, Department of Geology, Faculty of Geology and Geophysics, University of Bucharest, 1 N. Bălcescu Bd, 010041 Bucharest, Romania.
Emails: mihaela.gradinaru@unibuc.ro (M.G.); iuliana.lazar@g.unibuc.ro (I.L.)

Funding information
Research Institute of the University of Bucharest (ICUB), Grant/Award Number: 28544/2017; Romanian Executive Agency for Higher Education, Research, Development and Innovation Funding (UEFISCDI) project, Grant/Award Number: PN-III-P4-ID-PCCF-2016-0014

Abstract

Ferruginous stromatolites occur associated with Middle Jurassic condensed deposits in several Tethyan and peri-Tethyan areas. The studied ferruginous stromatolites occurring in the Middle Jurassic condensed deposits of Southern Carpathians (Romania) preserve morphological, geochemical, and mineralogical data that suggest microbial iron oxidation. Based on their macrofabrics and accretion patterns, we classified stromatolites: (1) Ferruginous microstromatolites associated with hardground surfaces and forming the cortex of the macro-oncoids and (2) Domical ferruginous stromatolites developed within the *Ammonitico Rosso*-type succession disposed above the ferruginous microstromatolites (type 1). Petrographic and scanning electron microscope (SEM) examinations reveal that different types of filamentous micro-organisms were the significant framework builders of the ferruginous stromatolitic laminae. The studied stromatolites yield a large range of δ^{56}Fe values, from −0.75‰ to +0.66‰ with predominantly positive values indicating the prevalence of partial ferrous iron oxidation. The lowest negative δ^{56}Fe values (up to −0.75‰) are present only in domical ferruginous stromatolites samples and point to initial iron mobilization where the Fe(II) was produced by dissimilatory Fe(III) reduction of ferric oxides by Fe(III)-reducing bacteria. Rare-earth elements and yttrium (REE + Y) are used to decipher the nature of the seawater during the formation of the ferruginous stromatolites. Cerium anomalies display moderate to small negative values for the ferruginous microstromatolites, indicating weakly oxygenated conditions compatible with slowly reducing environments, in contrast to the domical ferruginous stromatolites that show moderate positive Ce anomalies suggesting that they formed in deeper, anoxic–suboxic waters. The positive Eu anomalies from the studied samples suggest a diffuse hydrothermal input on the seawater during the Middle Jurassic on the sites of ferruginous stromatolite accretion. This study presents the first interpretation of REE + Y in the Middle Jurassic ferruginous stromatolites of Southern Carpathians, Romania.

KEYWORDS

ferruginous stromatolites, iron isotopes, Jurassic, microbial signatures, rare-earth elements, Romania

1 | INTRODUCTION

Iron-rich sedimentary formations are widespread during the Archaean and Proterozoic but are restricted temporally and spatially during the Phanerozoic. Some of these formations feature clear stromatolitic textures. However, most of them do not show distinctive stromatolitic layering or microbialite textures. It has been suggested that the genesis of these deposits could be associated with global episodic geologic events, generated from interactions between geologic, geochemical and biological processes (Chan, Emerson, & Luther, 2016 and references therein). Here, we refer to Middle Jurassic ferruginous stromatolites, related to stratigraphic discontinuities and carbonate condensed successions in several Tethyan and peri-Tethyan areas. These ferruginous laminated textures usually form crusts associated with complex hardground surfaces and/or form the laminated cortex of macro-oncoids, oncoids, and ooids. Considering their diverse morphology, texture, and geochemistry, iron mineralized laminated structures associated with Middle-Upper Jurassic condensed successions have been reported in the literature under different terms such us: ferruginous microbialites (Burkhalter, 1995; Reolid & Abad, 2018), ferruginous stromatolites, microstromatolites (Gradziński, Tyszka, Uchman, & Jach, 2004; Jenkyns, 1971; Lazăr & Grădinaru, 2014; Lazăr, Grădinaru, & Petrescu, 2013; Mamet & Préat, 2003; Palmer & Wilson, 1990; Préat, Mamet, Ridder, Boulvain, & Gillan, 2000; Reolid & Nieto, 2010), and Fe-Mn dendrolitic structures (Böhm & Brachert, 1993; Kazmierczak & Kempe, 2006; Reolid & Molina, 2010).

The genesis of the iron-rich laminated deposits (e.g., banded iron formation, ferruginous stromatolites/microstromatolites) had long been a subject of many contradictory discussions and continues to be a topic of research interest. Numerous authors suggest that the genesis of the ferruginous stromatolites and banded iron formations could be related to the microbial activity that plays an important role in precipitation of iron compounds of these structures (e.g., Chan et al., 2016; Grădinaru, 2011; Gradziński et al., 2004; Konhauser et al., 2002; Krepski, Emerson, Hredzak-Showalter, Luther, & Chan, 2013; Lazăr & Grădinaru, 2014; Lazăr et al., 2013; Mamet & Préat, 2003; Palmer & Wilson, 1990; Planavsky et al., 2009; Préat, Jong, Mamet, & Mattielli, 2008; Reolid & Nieto, 2010; Salama, Aref, & Gaupp, 2013; Shapiro & Konhauser, 2015). Others suggested a diagenetic origin of these structures (e.g., Sandoval & Checa, 2002). However, the formation mechanisms of iron-rich stromatolitic deposits are still widely debated.

In the recent decades, redox-sensitive tracers such as iron isotopes and rare-earth elements were used for the study of Proterozoic iron-rich stromatolites, suggesting that these ancient microbial benthic ecosystems were possibly dominated by microaerophilic iron-oxidizing bacteria as primary producers (Lin, Tang, Shi, Zhou, & Huang, 2019; Planavsky et al., 2009, 2012). Regarding the Middle Jurassic ferruginous stromatolites, there are only few studies concerning the textural, compositional features, geochemistry, mineralogy, and the environmental context of their genesis. These studies suggest a possible microbial origin (e.g., Burkhalter, 1995; Grădinaru, 2011; Lazăr et al., 2013; Mamet & Préat, 2003; Préat et al., 2008; Préat et al., 2000; Préat, Mamet, Stefano, Martire, & Kolo, 2011; Reolid, Abad, & Martín-García, 2008; Reolid & Molina, 2010; Reolid & Nieto, 2010) and only a few of them (Abad & Reolid, 2012; Préat et al., 2008; Reolid et al., 2008; Reolid & Nieto, 2010) report data concerning iron isotopes and REE content of such stromatolites structures.

Key points

- Morphological, geochemical, and mineralogical data from the ferruginous stromatolites suggest a microbial origin.
- Iron isotopes, rare-earth elements, and yttrium were used as palaeoenvironmental indicators.
- Eu anomalies indicate a diffuse hydrothermal input on the seawater during formation of Middle Jurassic ferruginous stromatolites.
- The lack of true negative Ce anomalies in the microfossiliferous ferruginous stromatolites suggests low oxygen conditions at water–sediment interfaces providing appropriate settings for microaerophilic Fe-oxidizing micro-organisms.

The aim of the present paper is to report new morphological, geochemical, and mineralogical data to decipher the paleoenvironmental context and to link micro-organisms to iron oxidation involved in the genesis of Middle Jurassic ferruginous stromatolites.

2 | GEOLOGICAL SETTING

The studied ferruginous stromatolites were recorded from the Middle Jurassic deposits of two major tectonic units of the Southern Carpathians (Figure 1a): a structurally higher, Getic Unit (or Median Dacides) and the lower, Danubian Unit (or Marginal Dacides) (Săndulescu, 1984). These represent a basement-dominated mid-Cretaceous fold and thrust belt resulting from the closure of a segment of the Alpine Tethys (Săndulescu, 1984, 1994). The sedimentary cover in the eastern part of the Getic Unit is

FIGURE 1 Location of the studied sections: (a) general location of the studied zones within the Southern Carpathians (based on the geotectonic map of Romania, Săndulescu, 1984). (b) Location of the section Strunga Pass on the geological outline map of the Bucegi Mountains (based on Patrulius, 1969). (c) Location of the section Purcărete Valley on the geological outline map of the Rucăr zone (based on Patrulius, 1969). (d) Location of the section Saraorschi Valley on the geological outline map of the Almăjului Mountains (based on Codarcea et al., 1966)

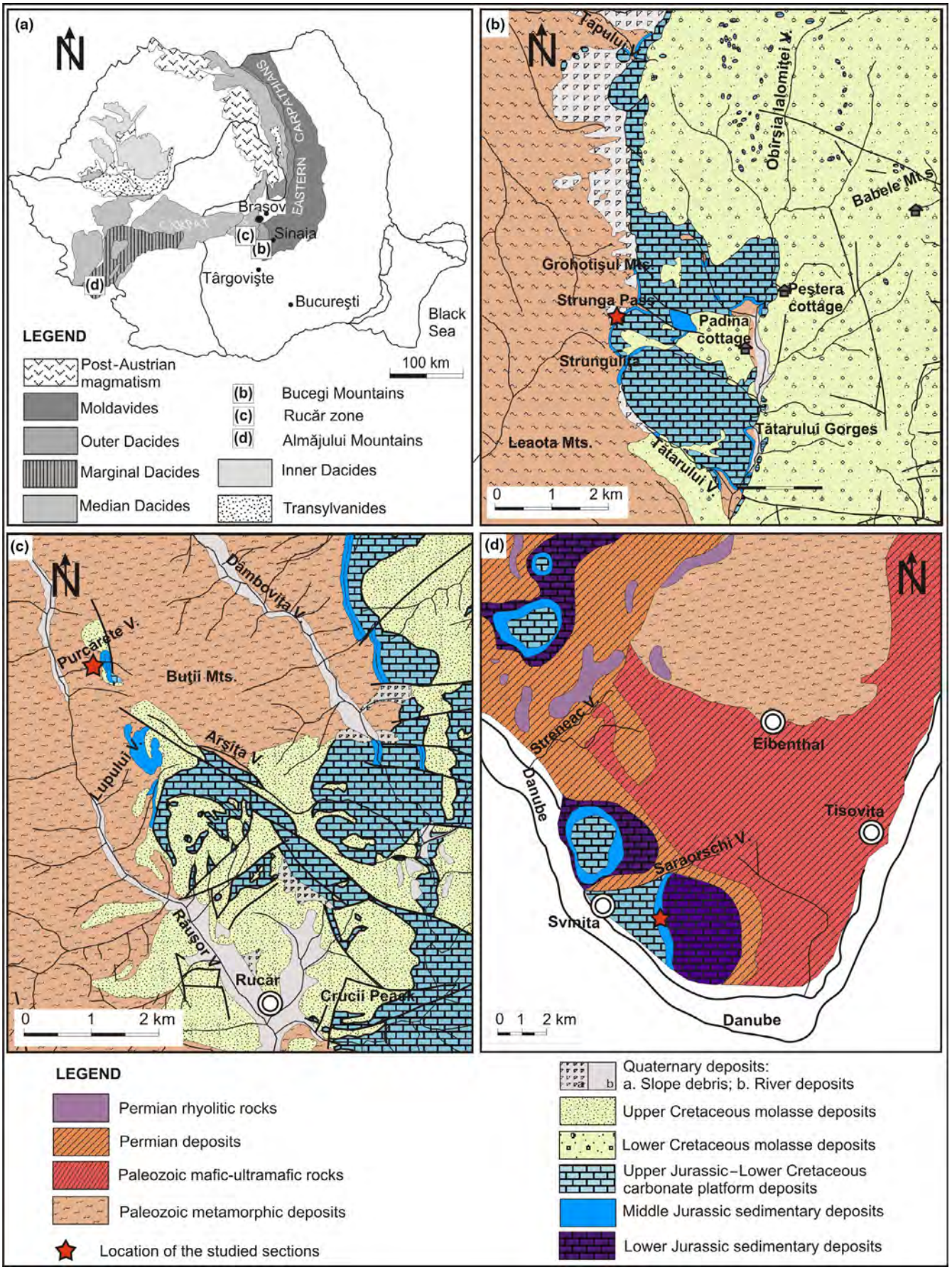
(a)
CARPATHIANS
EASTERN CARPATHIANS
Braşov
Sinaia
Târgovişte
Bucureşti
Black Sea
100 km
LEGEND
Post-Austrian magmatism
Moldavides
Outer Dacides
Marginal Dacides
Median Dacides
Inner Dacides
Transylvanides
(b) Bucegi Mountains
(c) Rucăr zone
(d) Almăjului Mountains
(b)
Grohotişul Mts.
Strunga Pass
Strungului
Leaota Mts.
Peştera cottage
Padina cottage
Tătarului Gorges
Babele Mts.
0 1 2 km
(c)
Dâmbovita V.
Purcărete V.
Buţii Mts.
Arşiţa V.
Lupului V.
Răuşor V.
Rucăr
Crucii Peack
0 1 2 km
(d)
Streneac V.
Eibenthal
Danube
Tisovita
Şaraorschi V.
Svinita
0 1 2 km
Danube
LEGEND
Permian rhyolitic rocks
Permian deposits
Paleozoic mafic-ultramafic rocks
Paleozoic metamorphic deposits
Location of the studied sections
Quaternary deposits: a. Slope debris; b. River deposits
Upper Cretaceous molasse deposits
Lower Cretaceous molasse deposits
Upper Jurassic–Lower Cretaceous carbonate platform deposits
Middle Jurassic sedimentary deposits
Lower Jurassic sedimentary deposits

represented by Triassic–Lower Cretaceous sediments. They are resting on a peri-Gondwanan terrane composed of Cambro-Silurian island arcs (Balintoni, Balica, Ducea, & Hann, 2014) metamorphosed during two distinct events in the Paleozoic (Ducea et al., 2016). The Danubian Units consist of several variably metamorphosed arc terranes of pan African affinity (Balintoni et al., 2014) and un-metamorphosed granitic rocks of earliest Permian age as well as Paleozoic cover rocks. Unlike the basement units of the Getic realm, there is no Variscan or younger metamorphism in the Danubian, in all making these basement terrains quite distinctive. Both represent continental margin rocks to the Jurassic Severin basin and both were covered by Upper Jurassic–Lower Cretaceous carbonate platforms prior to their juxtaposition during the mid-Cretaceous. The facies of the Jurassic to Lower Cretaceous sedimentary series reveal a complex paleogeography of the Danubian realm and were described by numerous authors starting with Răileanu (1953, 1960), Popa, Năstăseanu, and Antonescu (1977) Năstăseanu (1979) among others and a synthesis was presented by Grădinaru in Haas et al., 2011 and references therein).

During the Middle Jurassic, some areas of these units (e.g., Bucegi Mountains, Rucăr zone in the Getic unit) accumulated mixed carbonate–siliciclastic condensed deposits characterized by reduced stratigraphic thickness (less than one meter to few tens of meters) compared with the stratigraphic thickness of the contemporaneous expanded successions (of hundreds of meters, e.g., Reșita-Moldova Nouă area in the western part of the Getic unit in the Southern Carpathians). These successions contain condensed beds associated with diachronous hardgrounds which reveal signs of reduced sedimentation rates, omission, erosion, in situ reworking, taphonomic condensation, and synsedimentary cementation (Lazăr et al., 2013).

Three Middle Jurassic sections from the Southern Carpathians have been studied: Strunga Pass (Bucegi Mountains, Figure 1b), Purcărete Valley (Rucăr zone, Figure 1c) from Getic Unit and Saraorschi Valley (Almăjului Mountains, Figure 1d) from Danubian Units.

Strunga Pass is located on the western slope of the Bucegi Mountains. The biostratigraphy and lithostratigraphy of this section were presented in detail by Patrulius (1969) and Lazăr (2006). The lower part of the succession is represented by yellowish ooidal bioclastic grainstone and ooidal bioclastic grainstone–packstone (2.5–5.5 m thick) with thin, discontinuous, quartzitic micro-conglomerate intercalations (Figures 2a and 3a,h). The top of these deposits is marked by a sharp hardground discontinuity (Figures 2a and 3a). The next bed (0.65–1 m thick) has a nodular aspect and consists of oncoidal floatstone, respectively, gray-green to reddish bioclastic ooidal packstone–grainstone (Figures 2a–d and 3e–g) with cavities and fractures lined by Fems (type 1) and filled with bioclastic wackestone–packstone (Figures 2a and 3b,d). This bed contains numerous ferruginous macro-oncoids (Figures 2b–e and 3e), ferruginous ooids and a fossil assemblage with ammonites, belemnites along with representatives of benthic faunas (rare sponges, bivalves, gastropods, brachiopods, echinoids, crinoids, and extremely rare solitary corals; Lazăr et al., 2013). The top of this bed is represented by an uneven discontinuity hardground surface connected to cavities, fissures, and fractures developed within the underlying bed (Figure 2a,c,d). The hardground surface and the walls of the cavities and fissures are encrusted with 0.5- to 3-cm-thick ferruginous microstromatolites (Fems) (Figures 2b–e and 3d–g). This last unit represents a condensed bed corresponding to the Early Bathonian–Early Callovian time interval considering the ammonite fauna accumulated in this bed (cf. Patrulius, 1969). The mixture of non-contemporaneous fossil specimens (belonging to several biozones) with different degrees of preservation, as well as the occurrence of macro-oncoids that have nuclei represented by ammonite steinkerns with different preservation states, indicate faunal condensation (sensu Fürsich, 1978) and taphonomic condensation (sensu Gómez & Fernández-López, 1994). The overlying unit (1–2.5 m thick) is represented by red marly limestones with rhyncholites and foraminifera (Figure 3b) (Middle Callovian–Oxfordian, Neagu, Manea, & Gavrilescu, 1983), followed by 0.5- to 1-m-thick Middle Oxfordian jasper, radiolarites and 0.8-m-thick cherty limestones (Beccaro & Lazăr, 2007).

In the Rucăr zone, the Middle Jurassic succession from Purcărete Valley (Figure 4a) (a tributary of Râușor Valley) comprises of mixed siliciclastic–carbonate rocks (coarse sandstones and fine grained sandy limestones with discontinuous quartzite conglomerate intercalations; 16–21 m thick), followed upwards by yellowish bioclastic ooidal limestones (packstone–grainstone mixed with quartz and feldspar grains, Figure 4i, 2.5–5.5 m thick). The top of this unit is marked by a sharp hardground discontinuity, encrusted, with 1- to 2-cm-thick ferruginous crusts (Figures 2f and 4h) yielding agglutinated polychaete worm tubes, rare bryozoan colonies, crinoid ossicles, echinoid spines, small solitary corals, barnacles, fragmented belemnites, and reworked ammonites, along with ferruginous macro-oncoids and abundant ferruginous ooids (Lazăr & Grădinaru, 2014). The overlying bed (0.7–0.8 m thick) consists of gray–green to yellowish bioclastic ooidal packstone–grainstone and oncoidal floatstone (Figure 4f,g). This bed reveals numerous cavities and fractures filled with bioclastic packstone (Figure 2f). The nodular aspect of this bed is generated by the numerous ferruginous macro-oncoids (ranging from 1 up to 7 cm in diameter); the bed contain also numerous ferruginous ooids, reworked ammonites, belemnites, crinoids, oysters, along with rare gastropods, brachiopods, echinoids, sponges, and solitary corals (Figure 4f). This bed represents a condensed unit corresponding to the (?)Bathonian–Callovian interval (Patrulius, 1969; Patrulius et al., 1980). The early lithification of the condensed unit is evidenced by the precipitation of several types of early cement (isopachous fibrous and radiaxial cements), which appear synchronously with the colonization of the substrate by the macro- and microfauna. The top of the condensed bed is marked by a second, uneven hardground discontinuity covered by 0.5- to 2-cm-thick Fems (Figure 4f). The next unit is represented by green-red bioclastic packstone with ammonites (1.6 m thick, Figure 4d,e), red to pink microbial bioclastic packstone (0.86 m thick, Figure 4b,c) containing coarse to medium sized, angular rock fragments derived

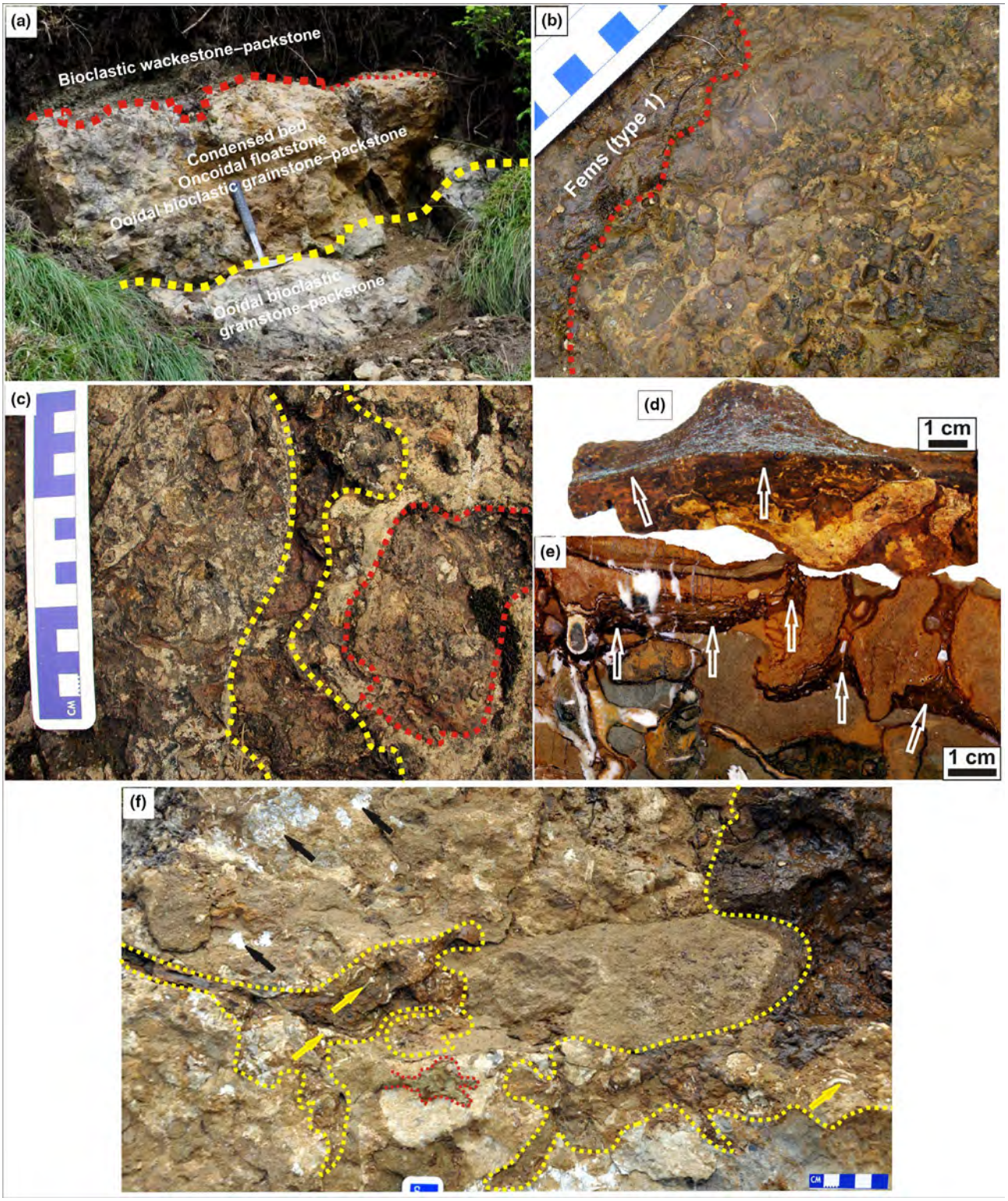

FIGURE 2 (a–e) Bucegi Mountains: (a) outcrop view of the oncoid-bearing condensed bed bounded by two sharp discontinuities (dotted lines); red dotted line indicate the hardground surface encrusted by Fems; (b, c) surface view of the oncoid-bearing condensed bed encrusted with Fems (type 1); (c) fracture encrusted with Fems (yellow dotted line); dotted red line outlines a macro-oncoid; (d) uneven hardground surface encrusted with 0.5- to 3-cm-thick Fems crust (white arrows); (e) polished slab on the oncoid-bearing condensed bed showing cavities filled with Fems (type 1) (white arrows); (f) Rucăr zone (Purcărete Valley): surface view of the oncoid-bearing condensed bed: yellow dotted lines outline the irregular cavities filled with ferruginous microstromatolites (Fems, type 1) containing agglutinated worm tubes (yellow arrows); irregular cavity encrusted with Fems and filled with green bioclastic packstone (red dotted lines); black arrows indicate fragments of large bivalves shells encrusted by Fems

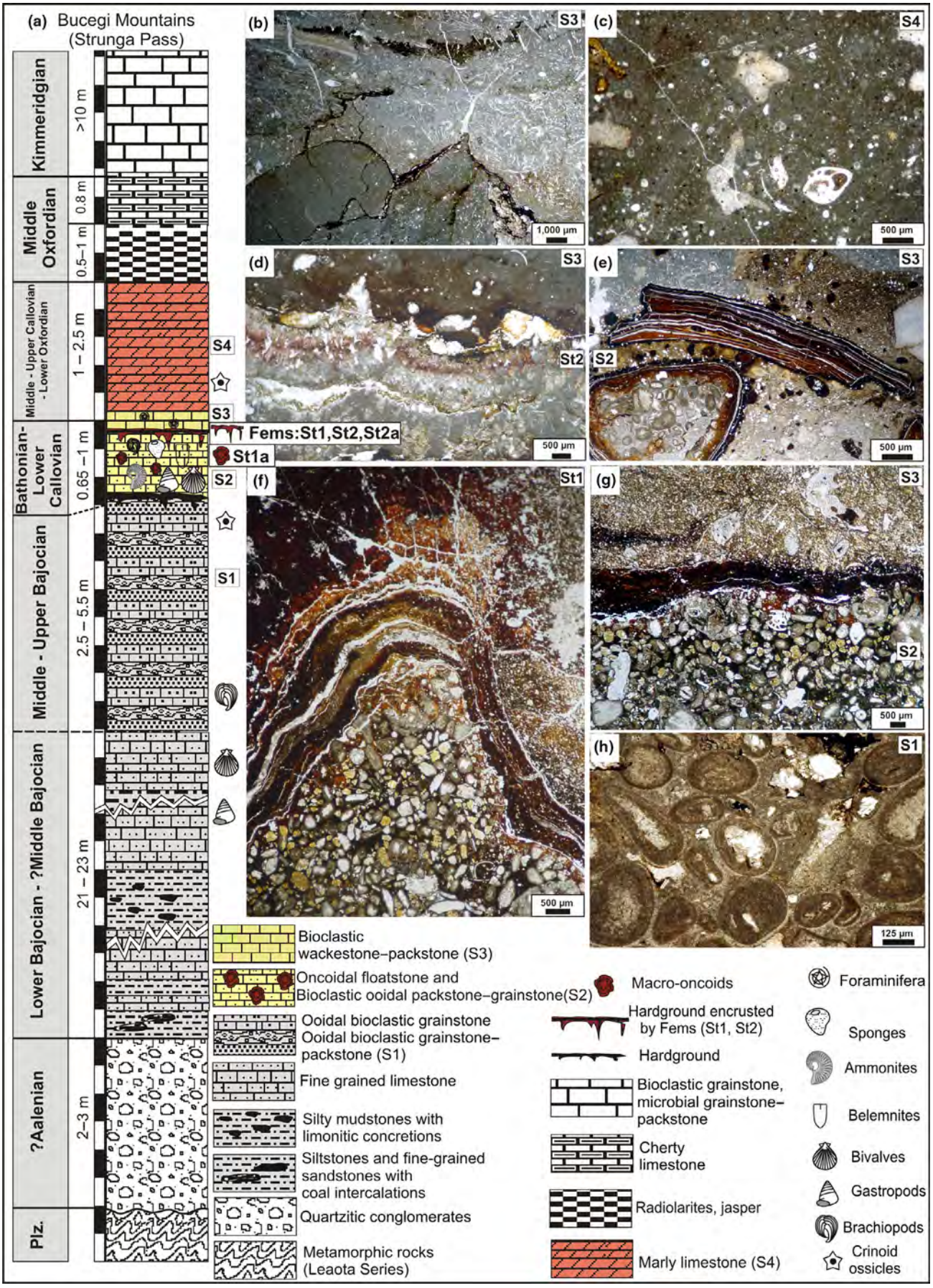
(a) Bucegi Mountains (Strunga Pass)
Kimmeridgian
>10 m
Middle Oxfordian
0.8 m
0.5–1 m
Middle - Upper Callovian - Lower Oxfordian
1 – 2.5 m
Bathonian-Lower Callovian
0.65 –1 m
Middle - Upper Bajocian
2.5 – 5.5 m
Lower Bajocian - ?Middle Bajocian
21 – 23 m
?Aalenian
2–3 m
Plz.
S4
S3
Fems:St1,St2,St2a
St1a
S2
S1
(b) S3 1,000 µm
(c) S4 500 µm
(d) S3 St2 500 µm
(e) S3 S2 500 µm
(f) St1 500 µm
(g) S3 S2 500 µm
(h) S1 125 µm
Bioclastic wackestone–packstone (S3)
Oncoidal floatstone and Bioclastic ooidal packstone–grainstone(S2)
Ooidal bioclastic grainstone
Ooidal bioclastic grainstone–packstone (S1)
Fine grained limestone
Silty mudstones with limonitic concretions
Siltstones and fine-grained sandstones with coal intercalations
Quartzitic conglomerates
Metamorphic rocks (Leaota Series)
Macro-oncoids
Hardground encrusted by Fems (St1, St2)
Hardground
Bioclastic grainstone, microbial grainstone–packstone
Cherty limestone
Radiolarites, jasper
Marly limestone (S4)
Foraminifera
Sponges
Ammonites
Belemnites
Bivalves
Gastropods
Brachiopods
Crinoid ossicles

FIGURE 3 (a) Lithostratigraphic log of the studied outcrop in Strunga Pass (Bucegi Mountains) (modified from Lazăr et al., 2013); (b–h) microphotographs of the representative microfacies in the studied section: (b) bioclastic wackestone–packstone; (c) marly limestone (bioclastic wackestone–packstone); (d) ferruginous microstromatolites growing downward from the walls of a cavity filled with bioclastic wackestone–packstone; note the calcite pinnacles grew on the base of the stromatolitic laminae; (e) oncoidal floatstone; (f, g) top of the condensed bed (here represented by bioclastic ooidal packstone–grainstone) affected by an uneven hardground surface encrusted with Fem; (h) ooidal bioclastic grainstone–packstone

from the underlying lithostratigraphic units and a mixture of numerous non-contemporaneous fossil specimens of ammonites from the Middle to Late Callovian time interval (Grigore, Lazăr, & Gheucă, 2015); these are followed by 1.25-m-thin-bedded pink limestones (bioclastic packstone–wackestone) and by Oxfordian cherty limestones (3–4 m thick).

The studied succession from Saraorschi Valley (Figure 6a) (a left tributary of the Danube River) belongs to the Danubian Units, Sirinia zone. The Jurassic deposits in this zone are represented by:

- Lower Jurassic calcareous–siliciclastic succession containing rich bivalves, brachiopods, nautiloids, and ammonite faunas developed within Late Sinemurian–Toarcian interval (Callomon & Grădinaru, 2005; Popa et al., 1977; Popa & Patrulius, 1996; Răileanu, 1953);
- The Middle Jurassic succession starts with whitish-gray quartz sandstones, assigned without paleontological data to the Aalenian by Răileanu (1953) and Popa et al. (1977). These are followed by Bajocian gray and cherry-red crinoidal grainstone–packstone (Figures 5d and 6i) and bioclastic ooidal packstone (Figure 6h) (almost 5–10 m thick), followed by a condensed bed (0.15–0.50 m thick) of Fe-ooidal oncoidal bioclastic limestones (Figures 5d,f and 6f,g) very rich in ammonites belonging to different biozones. The ammonite assemblage indicates Bathonian–Early Callovian time interval (cf. Năstăseanu, Bercia, Iancu, Vlad, & Hârtopanu, 1981; Patrulius & Popa, 1971; Răileanu, 1953, 1960) or the Middle Bathonian (cf. Galácz, 1994). This bed contains ferruginous macro-oncoids, and the top is marked by a hardground surface covered by Fems of type 1 (1–3 cm thick, Figure 5d). The condensed bed reveals early lithification evidenced by the precipitation of early cements such as syntaxial overgrowths surrounding echinoderm grains which are developed laterally and contemporaneously with the isopachous fibrous cement that surrounds the grains and intergranular spaces (Grădinaru, 2011). Just above the hardground encrusted with Fems (Figures 5d and 6g), other types of spectacular domical ferruginous stromatolites (DFeS) (type 2, Figures 5c,d,e and 6e) are developed, representing the base of the next unit composed of nodular red limestones (Figure 5a,b; *Ammonitico Rosso*-type, Middle-Upper Callovian, cf. Răileanu, 1953, Năstăseanu et al., 1981). These nodular limestones consist of bioclastic wackestone–packstones with planktonic bivalves, benthic (*Lenticulina*) and planktonic (*Protoglobigerina*) foraminifera, ostracods, radiolarians, peloids (Figure 6b,d). These are overlain by decimeter beds of grayish limestone and red or greenish limetones with cherts (Figure 6c, Oxfordian, cf. Năstăseanu et al., 1981).

3 | SAMPLES AND METHODS

In the studied sections, more than 250 samples have been collected from the condensed unit and the adjacent strata. Microfacies types and the meso- and microstructures of the ferruginous stromatolites were investigated in 120 thin sections under petrographic and binocular microscopes; 35 polished slabs were examined under cathodoluminescence (CL) microscopy. The chemical and mineralogical analyses were performed on 22 samples (Figure S1, supporting information) from all the studied sections.

The chemical and mineralogical composition was determined by X-ray fluorescence analysis (XRF), using a Horiba XGT 7000 device for major elements, and X-ray diffraction data, using a PANalytical's X'Pert PRO (microXRD) diffractometer. In addition, oriented clay aggregates were prepared and transferred on to a glass slide, dried at room temperature prior to X-ray scanning. Removal of calcite and separation of clay fractions were carried out according to Ostrum (1961). The samples have been also treated with ethylene glycol solvation and heated at 330 and 500°C to expand the smectite.

Rare-earth elements and yttrium (REE + Y) were determined in solution mode using a Thermo X-Series-2 Quadrupole Inductively Coupled Plasma-Mass Spectrometer at the University of Arizona (analytical details are presented in Rosel et al., 2013). Prior to analysis, sample aliquots were dissolved in mixtures of HF-HNO_3 ultra clean concentrated acids in a clean laboratory environment. Half of the sample aliquots were used for ICP-MS analyses and were re-dissolved in dilute HCl acid (1%) for introduction into the instrument nebulizer. The remainder of the sample was further processed for iron isotopic analysis. For REE + Y measurement, instrumental drift was corrected using Ru, In, and Re as internal standards. Uncertainties, calculated by repeated analyses of external standards (BCR-2), are ± 2%.

Aliquots for iron isotope measurements were passed through standard anion columns for chemical separation/purification after dissolution. Samples and standards were diluted to 3 ppm total iron. A Cu standard (JMC-ICP solution Specpure Lot No. 200536E) was added to each sample before analysis to a concentration of 3 ppm (Arnold, Weyer, & Anbar, 2004). Measurement of iron isotopes was performed at the University of Arizona on an ISOPROBE multicollector ICP-MS instrument. Measurements were performed in multicollector mode at the highest mass resolution following the procedures described elsewhere by Arnold et al. (2004). Each detector was positioned individually to discriminate the polyatomic interferences (mainly $^{40}Ar^{16}O^+$, $^{40}Ar^{16}OH^+$, and $^{40}Ar^{14}N^+$) at the edge of the detector slits so that only the undisturbed iron beams were detected.

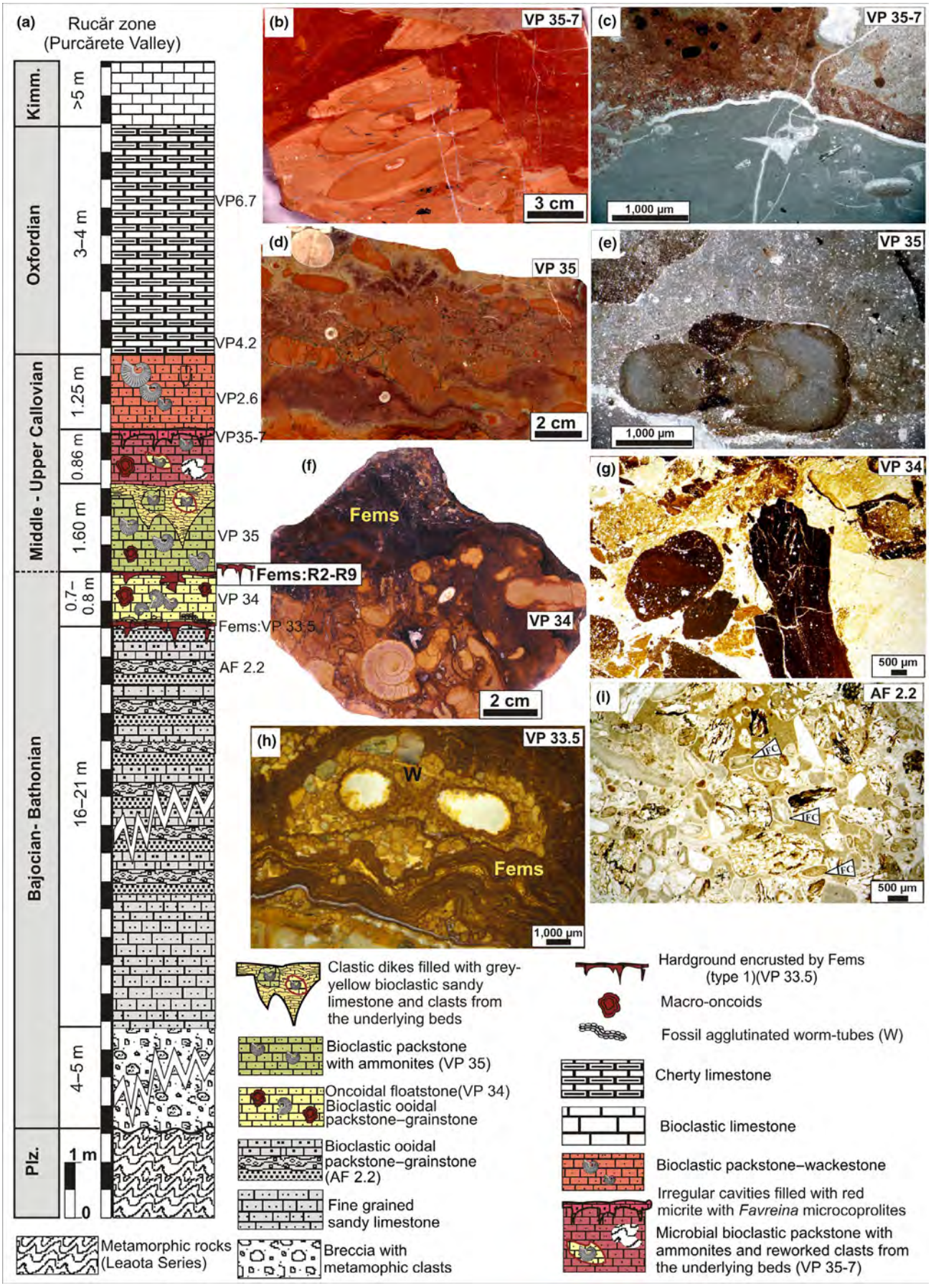
(a) Rucăr zone (Purcărete Valley)
Kimm.
Oxfordian
Middle - Upper Callovian
Bajocian- Bathonian
Plz.
>5 m
3–4 m
1.25 m
0.86 m
1.60 m
0.7–0.8 m
16–21 m
4–5 m
1 m
0
VP6.7
VP4.2
VP2.6
VP35-7
VP 35
Fems:R2-R9
VP 34
Fems:VP 33.5
AF 2.2
(b) VP 35-7
3 cm
(c) VP 35-7
1,000 µm
(d) VP 35
2 cm
(e) VP 35
1,000 µm
(f) Fems
VP 34
2 cm
(g) VP 34
500 µm
(h) VP 33.5
W
Fems
1,000 µm
(I) AF 2.2
FC
500 µm
Clastic dikes filled with grey-yellow bioclastic sandy limestone and clasts from the underlying beds
Bioclastic packstone with ammonites (VP 35)
Oncoidal floatstone(VP 34)
Bioclastic ooidal packstone–grainstone
Bioclastic ooidal packstone–grainstone (AF 2.2)
Fine grained sandy limestone
Breccia with metamophic clasts
Metamorphic rocks (Leaota Series)
Hardground encrusted by Fems (type 1)(VP 33.5)
Macro-oncoids
Fossil agglutinated worm-tubes (W)
Cherty limestone
Bioclastic limestone
Bioclastic packstone–wackestone
Irregular cavities filled with red micrite with Favreina microcoprolites
Microbial bioclastic packstone with ammonites and reworked clasts from the underlying beds (VP 35-7)

FIGURE 4 (a) Lithostratigraphic log of the studied outcrop in Purcărete Valley (Rucăr zone) (modified from Lazăr & Grădinaru, 2014); (b, c) microbial bioclastic packstone with ammonites and reworked metamorphic clasts; the top of this bed is affected by neptunian dikes filled with peloidal bioclastic packstone to grainstone with *Favreina* microcoprolites; (d, e) green-red bioclastic packstone with ammonites and belemnites; (f, g) oncoid-bearing condensed bed (bioclastic ooidal packstone–grainstone and oncoidal floatstone) encrusted with Fems (type 1); (h) ferruginous microstromatolites (Fems, type 1) and the agglutinated worm tubes (W) assemblages encrusting an ammonite steinkern; (i) packstone–grainstone mixed with quartz and feldspar grains surrounded by isopachous fibrous cement (IFC)

With the ISOPROBE mass resolution entrance slit, a resolving power of 8,000–9,000 is achieved. This is sufficient to fully resolve polyatomic interferences, which differ from the respective iron isotopes by less than 4,000 M/ΔM and to produce flat top peak sections enabling high-precision measurements. This includes all likely interferences except $^{56}FeH^+$, which is not fully resolved from $^{57}Fe^+$. Iron and Cu were measured in a dynamic mode, measuring all iron isotopes plus $^{53}Cr^+$ and $^{60}Ni^+$ in parallel during the first integration and the two Cu masses during the second integration. $^{53}Cr^+$ and $^{60}Ni^+$ were used to correct for potential isobaric interferences of $^{54}Cr^+$ and $^{58}Ni^+$ on $^{54}Fe^+$ and $^{58}Fe^+$, respectively. An assumed 63Cu/65Cu isotope ratio of 0.44563 of the Cu standard was used to correct for instrumental mass bias. The IRMM-014 standard was measured between every sample measurement. A blank measurement was made between every 4–5 samples. Other standards included a "gravimetric" iron standard. The gravimetric iron standard was prepared by the addition of a known amount of 54Fe tracer to a JMC-Fe standard. External precision on the $\delta^{56/54}Fe$ values is ~0.1 permil (2σ).

The organic matter and carbonate content were quantified by calculation of the weight loss during the reactions, measured by weighing the samples before and after heating at 105°C overnight to remove water, at 550°C for two hours to remove organic matter, and at 950°C for two hours to remove carbonates. The organic matter and carbonate content have been calculated using the equations: $LOI_{550} = [(DW_{105} - DW_{550})/DW_{105}] \times 100$ and $LOI_{950} = [(DW_{550} - DW_{950})/DW_{105}] \times 100$ (Heiri, Lotter, & Lemcke, 2001). In addition, carbon and oxygen stable isotope analyses of 18 carbonate powder samples were performed at the isotope laboratories of the Iso-Analytical Limited, United Kingdom. All the samples have been tested prior to isotope analysis with respect to potential diagenetic overprinting, using petrographic and cathodoluminescence microscopy as well as chemical data. Powdered samples were taken from polished slabs using a Dremel drill equipped with precision bits. The powdered samples were treated with 100% phosphoric acid at 75°C, and the evolved CO_2 was analyzed by Continuous Flow-Isotope Ratio Mass Spectrometry (CF-IRMS). All isotopic results are reported relative to the PDB (PeeDee Belemnite) standard (standard deviation smaller than 0.04%). Samples containing ferruginous stromatolites were examined directly under the SEM using backscattered electron imaging and energy-dispersive X-ray (EDS) spectroscopy microanalysis. The 25 SEM samples were cut perpendicular to the bedding, mounted on stubs and polished. Subsequently, the samples for SEM analysis were etched in 5% HCl for 15–25 s, and then, these were washed with distilled water, dried, and coated with gold. Etching of the sample after polishing was aimed to eliminate potential surface contamination.

4 | RESULTS

4.1 | Morphology of the ferruginous stromatolites

Two categories of ferruginous stromatolites were analyzed, based on their macrofabrics and accretion patterns, following the definitions and terminology proposed by Burkhalter (1995) and Lazăr et al. (2013): (1) Fems forming crusts with laminated macrofabric (3–30 mm thick) with planar to low-domal and columnar morphologies; (2) DFeS forming grouped coalescent clusters around 100–200 mm diameter and 20–60 mm high, with lobate to polygonal boundaries.

(1) Ferruginous microstromatolites show a general laminated macrofabric (10–30 mm thick on the hardground surfaces and 3–10 mm on the cortex of the macro-oncoids) (Figure 7a–c). The laminae are developed in several growth phases: from planar to low-domal, followed by columnar to wrinkled or wavy growth forms (Figure 7b–f). The planar to low-domal lamination consists of alternating light red to dark brown or green laminae (5 to 300 μm thick) and white to light yellow laminae (10–50 μm thick) (Figure 7d). The microstructure consists of dense iron-rich micrite and/or a meshwork of iron-rich micropeloids variously arranged parallel to the laminae, forming clusters, or showing an irregular laminated fabric. The white calcite laminae (10–50 μm thick) are composed of sparite and occur at irregular intervals. The columnar to wrinkle or wavy morphology shows faint irregular laminated fabric, suggested by color and texture variations of dense ferruginous micrite, clusters of irregular micropeloids, and diffuse meshwork of microfilaments (Figure 7g,h). This type of Fe microstromatolites was described in detail in terms of their morphology, dimensions, macrofabrics, and microfabrics by Lazăr et al. (2013).

Petrographical microscopy and scanning electron microscopy (SEM) revealed the microstructure of the Fems. The iron-rich laminae contain slightly curved filaments, with a diameter of 0.7–4 μm and variable length, with complex branching, forming a net-like structure (Figures 7h and 8). The filamentous structures bifurcate at an apical branching node (Figure 8a–c,f). These filaments are abundant, locally forming a continuous film with Fe coating in the ferruginous-sparitic laminae. In several samples, the directional orientation of the filaments could be observed (Figure 8e). Some filaments show evidence of a twisting morphology. However, this feature has been partially obscured by Fe coating.

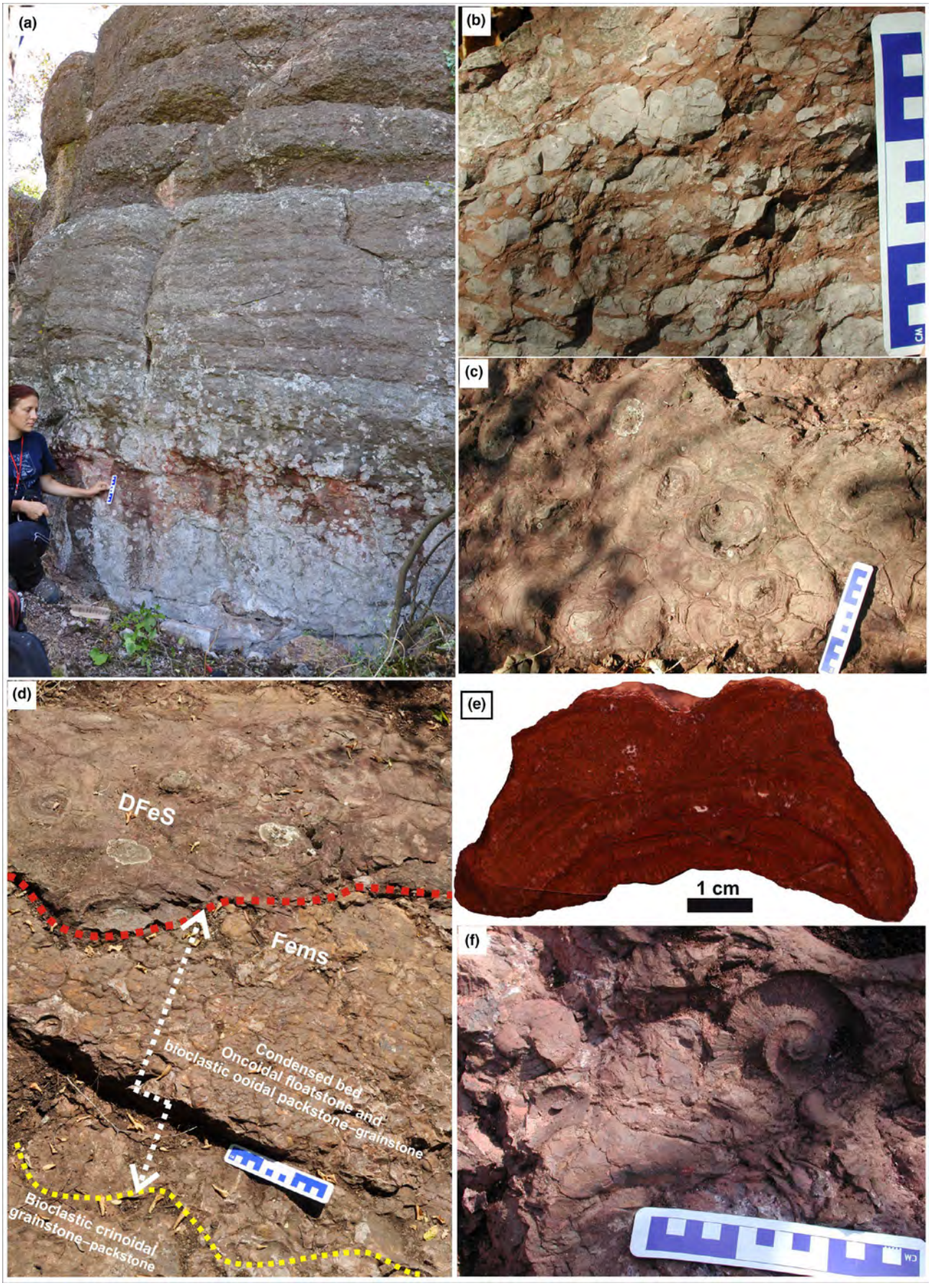
(a)
(b)
(c)
(d)
DFeS
Fems
Condensed bed
Oncoidal floatstone and
bioclastic ooidal packstone–grainstone
Bioclastic crinoidal
grainstone–packstone
(e)
1 cm
(f)

FIGURE 5 (a–f) Saraorschi Valley outcrop views: (a) Mihaela showing the base of the *Ammonitico Rosso*-type limestones, where the domical stromatolites occur; (b) nodular limestones (*Ammonitico Rosso*-type); (c) surface view of the domical ferruginous stromatolites (type 2); (d) outcrop view of the condensed bed encrusted by Fems (type 1) overlaid by DFeS (type 2); (e) polished surface through a domical stromatolite; (f) surface view of the oncoid-bearing condensed bed with ammonites, encrusted by Fems (type 1)

(2) Domical ferruginous stromatolites form coalescent clusters with lobate to polygonal boundaries (Figures 5c,e and 9a,b). These DFeS reveal large variations of meso- and microfabrics, ranging from distinctly laminated to irregularly laminated or structureless (Figure 9c–h). The basic stromatolitic microstructure is represented by alternating thin irregular wavy or wrinkle laminae of dense iron-rich micrite (0.04–0.2 mm thick, Figure 9e–h) and thicker micropeloidal laminae and intercalations of bioclastic wackestone–packstone with planktonic bivalves shells, *Protoglobigerinids* planktonic foraminifera, ostracods, and radiolarians (0.4–2 mm thick, Figure 9d,f,h). The lamination is also highlighted by the planktonic bivalves shells oriented parallel with the micritic laminae (Figure 9d,e,h). A distinct feature of the DFeS is represented by ferruginous structures with columnar multilobate to dendritic or club-shaped meso-morphologies, developed within the bioclastic wackestone–packstone intercalations (Figure 9e,g) and in the shelter cavities (pores) generated by the stromatolitic laminae (Figure 9g). These ferruginous structures are very similar to the morphotype of *Frutexites* described by Böhm and Brachert (1993). *Frutexites*-like shrubs grow perpendicular on laminations and are often fixed on these planktonic bivalves shells (Figure 9e,g).

The microstructure of DFeS reveals the presence of slightly curved filaments of 1–1.5 μm width and 50 –100 μm maximum observed length, forming a dense network within the ferruginous laminae (Figure 10a–f); filaments show dichotomous branching at apical nodes (Figure 10f).

4.2 | Mineralogy

X-ray diffraction analysis (XRD) of the Fems showed that goethite is the most ferriferous component in all the studied samples. Hematite and magnetite are subordinate. Furthermore, XRD data showed the presence of calcite, quartz, and low amounts of fluorapatite. In the DFeS samples, the XRD data reveal significant amounts of hematite with subordinate quantities of goethite and magnetite as iron phases. Other mineral assemblages identified under XRD are calcite and quartz. The clay minerals identified by the XRD patterns obtained from oriented aggregates indicate the presence of illite, montmorillonite, kaolinite, and chlorite in all the studied samples.

4.3 | Geochemistry

4.3.1 | X-ray fluorescence analyses

Samples from both types of stromatolites (Fems and DFeS) consist mainly of iron-rich carbonates with Fe_2O_3 concentrations that vary from 64.22% to 88.55% with an average of 74.84%. Other main components were also detected, such as CaO, SiO_2, Al_2O_3, P_2O_5, MgO, K_2O, TiO_2, and MnO (Table 1).

4.3.2 | Energy-dispersive X-ray spectroscopy (EDS)

Chemical data performed by electron-microprobe analyses done on the filamentous microstructures identified within the laminae of both types of stromatolites (Fems and DFeS) reveal a notable presence of Fe, Ca, Si, and Al.

4.3.3 | Iron isotope analysis

Iron isotope data have been performed on 22 samples for both types of ferruginous stromatolites (Fems and DFeS) from all the studied sections and are shown in Figure 11 and reported in Table 1. δ^{56}Fe values of Fems samples ranged from −0.20‰ to +0.66‰, with predominantly positive values. In Saraorschi Valley, the DFeS have exclusively negative δ^{56}Fe values ranging from −0.05‰ to −0.75‰.

4.3.4 | Calcium carbonate and total organic carbon

The calcium carbonate contents vary from 0.97% to 72% whereas the total organic carbon (TOC) ranging from 0.22% to 2.62%, with an average of 1.10% in both types of ferruginous stromatolites. The Fems from all the studied samples range from 0.97% to 4.42% carbonate content and show the overall highest TOC contents, ranging from 1.6% to 2.51% with a mean of 2.18%. Significant differences in the DFeS samples are reflected in the higher carbonate content (up to 72% with an average of 58.28%) and very low TOC concentrations, not exceeding 0.39%.

4.3.5 | Carbon and oxygen stable isotope analyses

Stable isotope studies of δ^{13}C and δ^{18}O in ferruginous stromatolites have been used primarily to define depositional environments and assess the degree of alteration during diagenesis. 18 samples selected for isotopic analyses were taken from the ferruginous stromatolites (Fems and DFeS) from all the three sections. Analyses show that δ^{13}C values of the Fems and DFeS range from 1.64‰ to 2.95‰ (Figure 12, Table 2) whereas δ^{18}O values for the same samples vary from −0.41‰ to −4.19‰. The average δ^{13}C values from Fems and DFeS systematically exhibit a positive

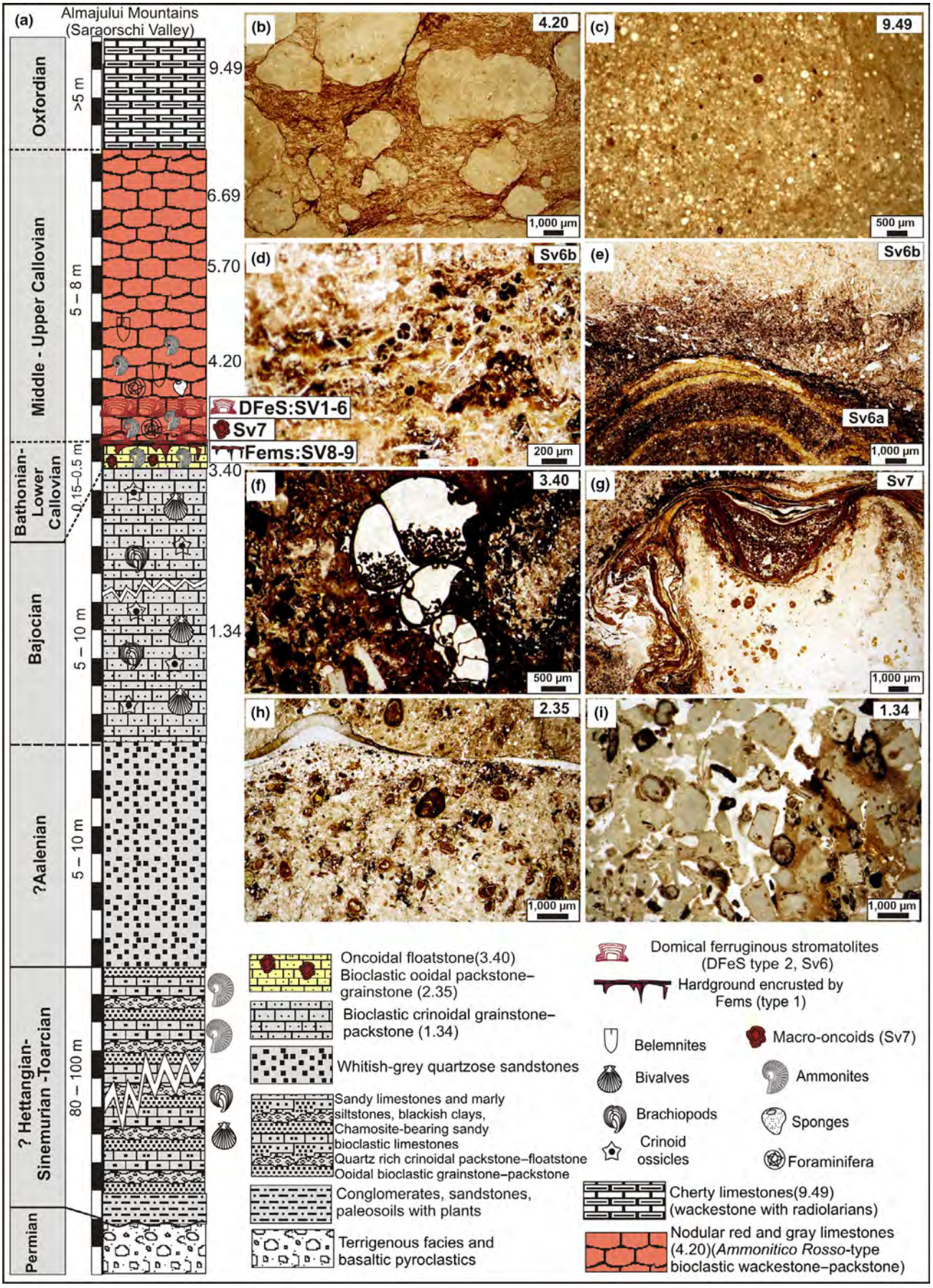
(a)
Almajului Mountains
(Saraorschi Valley)
Oxfordian
>5 m
Middle - Upper Callovian
5 – 8 m
Bathonian-Lower Callovian
0.15–0.5 m
Bajocian
5 – 10 m
?Aalenian
5 – 10 m
? Hettangian-Sinemurian -Toarcian
80 – 100 m
Permian
9.49
6.69
5.70
4.20
3.40
1.34
DFeS:SV1-6
Sv7
Fems:SV8-9
(b) 4.20
1,000 µm
(c) 9.49
500 µm
(d) Sv6b
200 µm
(e) Sv6b
Sv6a
1,000 µm
(f) 3.40
500 µm
(g) Sv7
1,000 µm
(h) 2.35
1,000 µm
(i) 1.34
1,000 µm
Oncoidal floatstone(3.40)
Bioclastic ooidal packstone–grainstone (2.35)
Bioclastic crinoidal grainstone–packstone (1.34)
Whitish-grey quartzose sandstones
Sandy limestones and marly siltstones, blackish clays, Chamosite-bearing sandy bioclastic limestones
Quartz rich crinoidal packstone–floatstone
Ooidal bioclastic grainstone–packstone
Conglomerates, sandstones, paleosoils with plants
Terrigenous facies and basaltic pyroclastics
Domical ferruginous stromatolites (DFeS type 2, Sv6)
Hardground encrusted by Fems (type 1)
Belemnites
Bivalves
Brachiopods
Crinoid ossicles
Macro-oncoids (Sv7)
Ammonites
Sponges
Foraminifera
Cherty limestones(9.49) (wackestone with radiolarians)
Nodular red and gray limestones (4.20)(*Ammonitico Rosso*-type bioclastic wackestone–packstone)

FIGURE 6 (a) Lithostratigraphic log of the studied outcrop in Saraorschi Valley (Almăjului Mountains); (b) nodular red limestones (*Ammonitico Rosso*-type); (c) radiolarians wackestone; (d) bioclastic wackestone–packstones with planktonic bivalves and *Protoglobigerinids*; (e) domical ferruginous stromatolites (type 2); (f, g) bioclastic ooidal packstone–grainstone and oncoidal floatstone; (g) Fems (type 1) encrusting the hardground surface; (h) Bioclastic ooidal packstone; (i) crinoidal grainstone–packstone

trend while the average $\delta^{18}O$ values gradually become more negative from Fems toward DFeS samples. In the Strunga Pass samples, a cross-plot of carbon and oxygen isotopes revealed a narrow range of values: 2.05‰ to 2.14‰ for $\delta^{13}C$, and −0.41‰ to −1.50 ‰ for $\delta^{18}O$. Furthermore, in the Purcărete Valley samples, the $\delta^{13}C$ values fluctuate between 1.64‰ and 2.95‰ and −1.46‰ to −4.19‰ for the $\delta^{18}O$, respectively. The $\delta^{13}C$ values of Fems from the Saraorschi Valley indicate positive values from 1.92‰ to 2.09‰ while DFeS samples show a positive trend, with values varying between 1.69‰ and 2.09‰, and $\delta^{18}O$ values range from −2.63‰ to −4.34‰ (Figure 12, Table 2).

4.3.6 | Rare-earth elements and yttrium

The concentration of the rare-earth elements and yttrium (REE + Y) of the Fems and DFeS are shown in Table 3. All REE + Y concentrations were normalized to post-Archean Australian Shale (PAAS, McLennan, 1989). The total REE (ΣREE) contents for all samples range from 17.66 to 144.69 ppm, with an average of 79.89 ppm. Significant variations in ΣREE content are distinguished in different types of ferruginous stromatolites. The Fems samples from the Purcărete Valley and Saraorschi Valley have highest concentration (30.58–144.69 ppm) of ΣREE whereas the Fems from Strunga Pass have lowest ΣREE content (20.11–25.94 ppm). In all the studied sections, the Fems display a wide range of light to heavy REE (LREE/HREE) ratios and display both negative and positive Cerium anomalies (Figure 13 and Table 3). Light to heavy REE ratios are calculated as the Pr_{SN}/Yb_{SN} ratio versus Ce anomalies (Figure 14a) and Y_{SN}/Y_{SN} ratio versus Cerium anomalies (Figure 14b) where SN represents normalization to Post-Archean Australian Shale (PAAS). Cerium anomalies (Ce/Ce^*), as defined in Figure 13, are calculated as $Ce/Ce^* = Ce_{SN}/(0.5La_{SN} + 0.5Pr_{SN})$ versus. $Pr/Pr^* = Pr_{SN}/(0.5Ce_{SN} + 0.5Nd_{SN})$; (cf. Bau & Dulski, 1996). The Fems samples display Ce values with slightly negative anomalies (with an average of 0.85 in the Strunga Pass) and an average of 0.80 in Saraorschi Valley. On the other hand, the Fems samples from Purcărete Valley display moderate negative Ce anomalies with an average of 0.55. Moreover, the DFeS samples from Saraorschi Valley record moderate positive Ce anomalies ranging from 1.04 to 1.62 (Figure 13 and Table 3). All the studied sections have positive Y/Y* anomalies (Figure 14b and Table 3). An average of Y/Ho ratio for Fems is 40.46 and 34.61 for DFeS samples. The Fems samples from the Strunga Pass show high Y/Ho ratios (ranging from 47.61 to 56.75 with an average of 52.55) whereas the Fems samples from Purcărete Valley show an average of 35.85 ppm. In the Saraorschi Valley, the values for Fems samples display an average of 38.18 ppm. Finally, Eu anomalies are calculated using $Eu/Eu^* = Eu_{SN}/(0.66Sm_{SN} + 0.33Tb_{SN})$ and displayed slightly negative to large positive data with values varying from 0.79 to 1.20, having an average of 1.07 ppm, in all the studied samples (Table 3).

5 | DISCUSSION AND INTERPRETATION

5.1 | Morphological biosignatures

Transmitted light microscopy and scanning electron microscopy (SEM) revealed the delicate microstructure of the studied ferruginous stromatolites composed of well-preserved three-dimensional reticulate networks and well-preserved filamentous bodies showing morphologies and dimensions suggestive of a possible microbial origin. Filamentous structures similar to those identified in the studied ferruginous stromatolites have been described from the Precambrian (Awramik & Baghoorn, 1977), Palaeozoic (Mamet, Préat, & DeRidder, 1997; Préat, Mamet, Bernard, & Gillan, 1999), and Mesozoic (Gradziński et al., 2004; Lazăr & Grădinaru, 2014; Lazăr et al., 2013; Mamet & Préat, 2003; Molina & Reolid, 2010; Préat et al., 2000; Reolid & Nieto, 2010). The width of the mineralized filamentous structures and the style of branching suggest similarities with mineralized tubular structures of *Zetaproteobacteria* microaerophilic Fe-oxidizing micro-organisms described by Krepski et al. (2013) and Chan et al. (2016). The studied iron-rich tubular filaments show a directional orientation within the microstromatolitic laminae (Figure 8a,e) similar to the results obtain by Krepski et al. (2013) in *Mariprofundus ferrooxydans* cultures, showing that this micro-organisms converge into a narrow (100–1,000 μm) growth bands and the stalks orient directionally in the band, elongating toward higher oxygen concentrations.

5.2 | Mineralogical biosignatures

Bacteria are major mediators in the deposition of many iron minerals such as ferrihydrite, goethite, hematite, or magnetite (cf. Mann, Tazaki, Fyfe, & Kerrich, 1992). In environments of low sedimentation rate and low oxygen concentration, situated below the photic zone microbes can play an important role, creating microenvironmental redox conditions, where Fe(II) is abundant leading to the formation of ferruginous minerals (Préat et al., 1999). Ferrihydrite is thought to be the first iron oxide that forms when aqueous ferrous iron is oxidized as a result of bacterial activity capable of coupling Fe(II) oxidation to nitrate reduction (cf. Benz, Brune, & Schink, 1998). The conversion of ferrihydrite to goethite

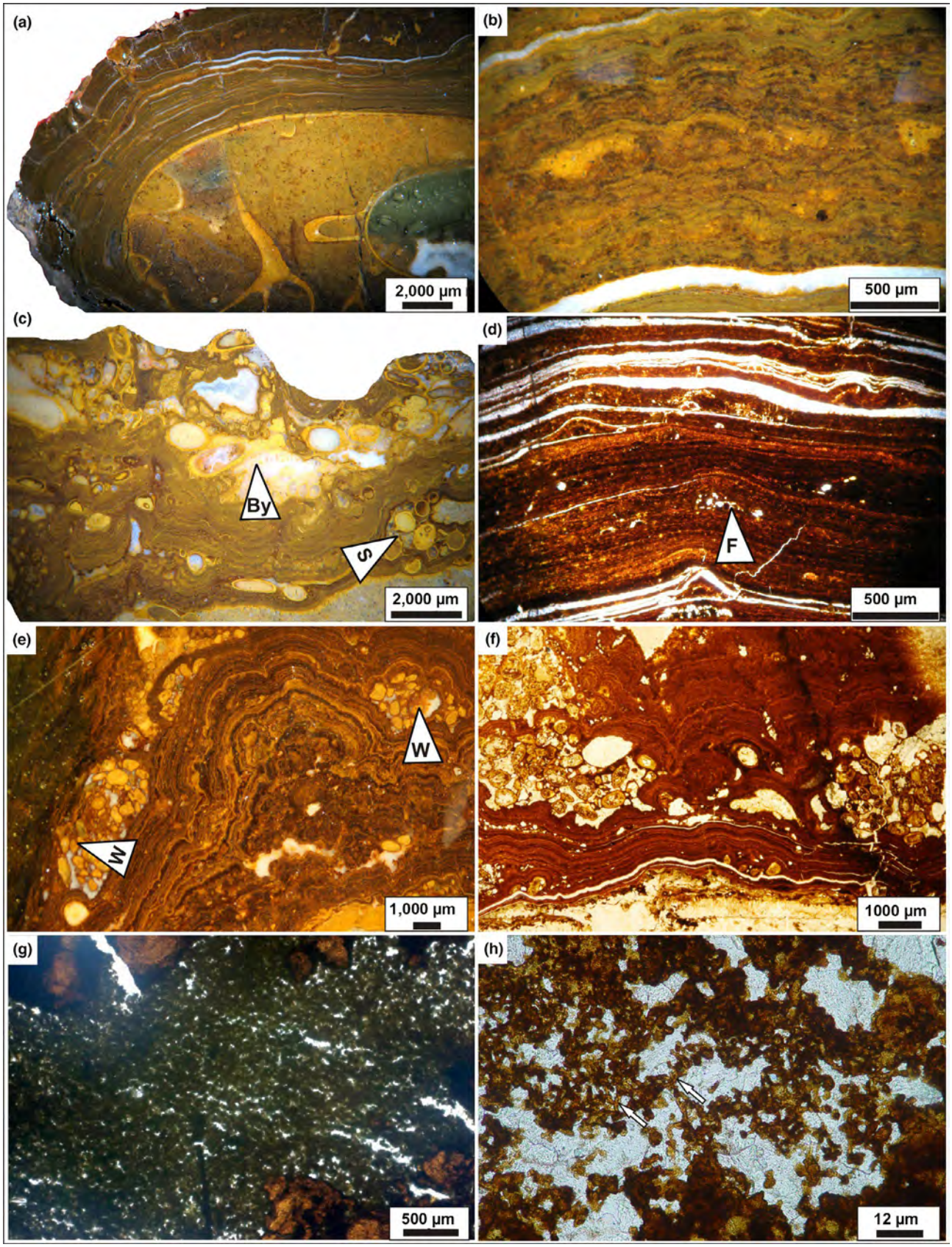

depends of temperature, pH, Eh, and Fe(II) concentrations (Préat et al., 1999; Schwertmann & Murad, 1983). Ferrihydrite is highly insoluble at circumneutral pH, and the conversion to goethite can only proceed in dysoxic–anoxic conditions in the presence of the ferrous iron (cf. Hansel et al., 2003). In the absence of ferrous iron, ferrihydrite will preferentially convert into hematite by

FIGURE 7 Morphology of the ferruginous microstromatolites (Fems): (a, b, e, f) Fems forming the cortex of the macro-oncoids; (a) the nucleus of the macro-oncoid is represented by an ammonite steinkern; (a, b) note the planar to low-domal sets of laminae, followed by columnar to wrinkled or wavy laminae; (c) Fems associated with the complex hardground surfaces; note the encrusting organism intergrowth within the iron laminae: serpulids (S) and bryozoans (By); (d) laminae of dense ferruginous micrite alternating at irregular intervals with sparitic laminae; note the presence of encrusting foraminifera (F) intergrowth within the laminae; (e) agglutinated worm tubes (W) within the iron laminae; (g) ferruginous laminae represented by dense ferruginous micrite or a meshwork of micropeloids; (h) filament-like cylindrical bodies composed of iron oxyhydroxides (arrow) observed within the columnar, wrinkled or wavy laminae

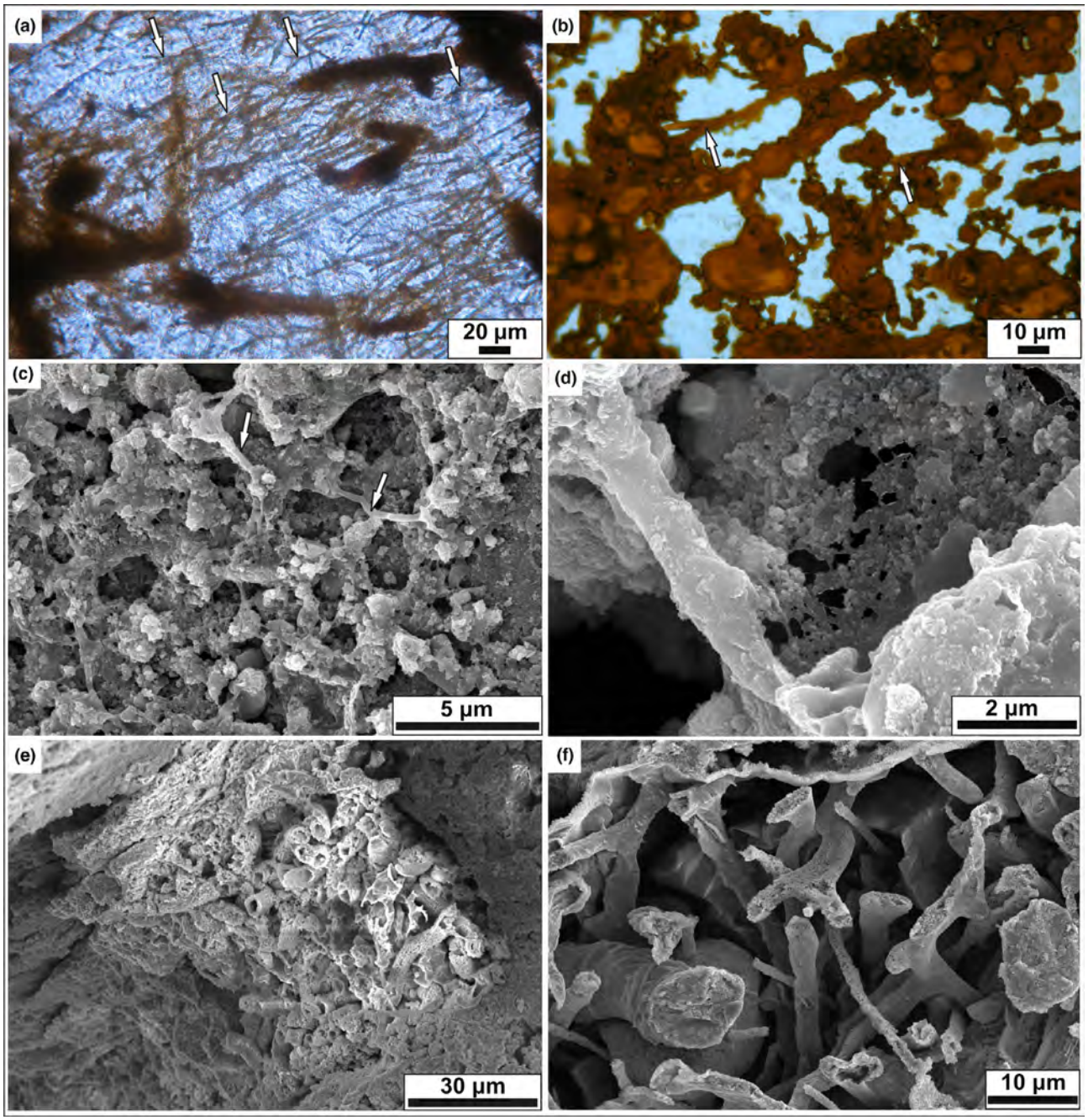

FIGURE 8 Microstructure of the ferruginous microstromatolites (Fems): thin sections (a, b) and SEM images (c–f) showing microfilaments with Fe coating forming a dense network within an iron-rich lamina of Fems; (a, b, c, f) filamentous structures (with a diameter of 0.7–4 µm) seem that are bifurcate at an apical branching node (arrows); (d) detail of a filament mineralized with solid, smooth Fe coating; (e) note the directional orientation of the dense clusters of filaments

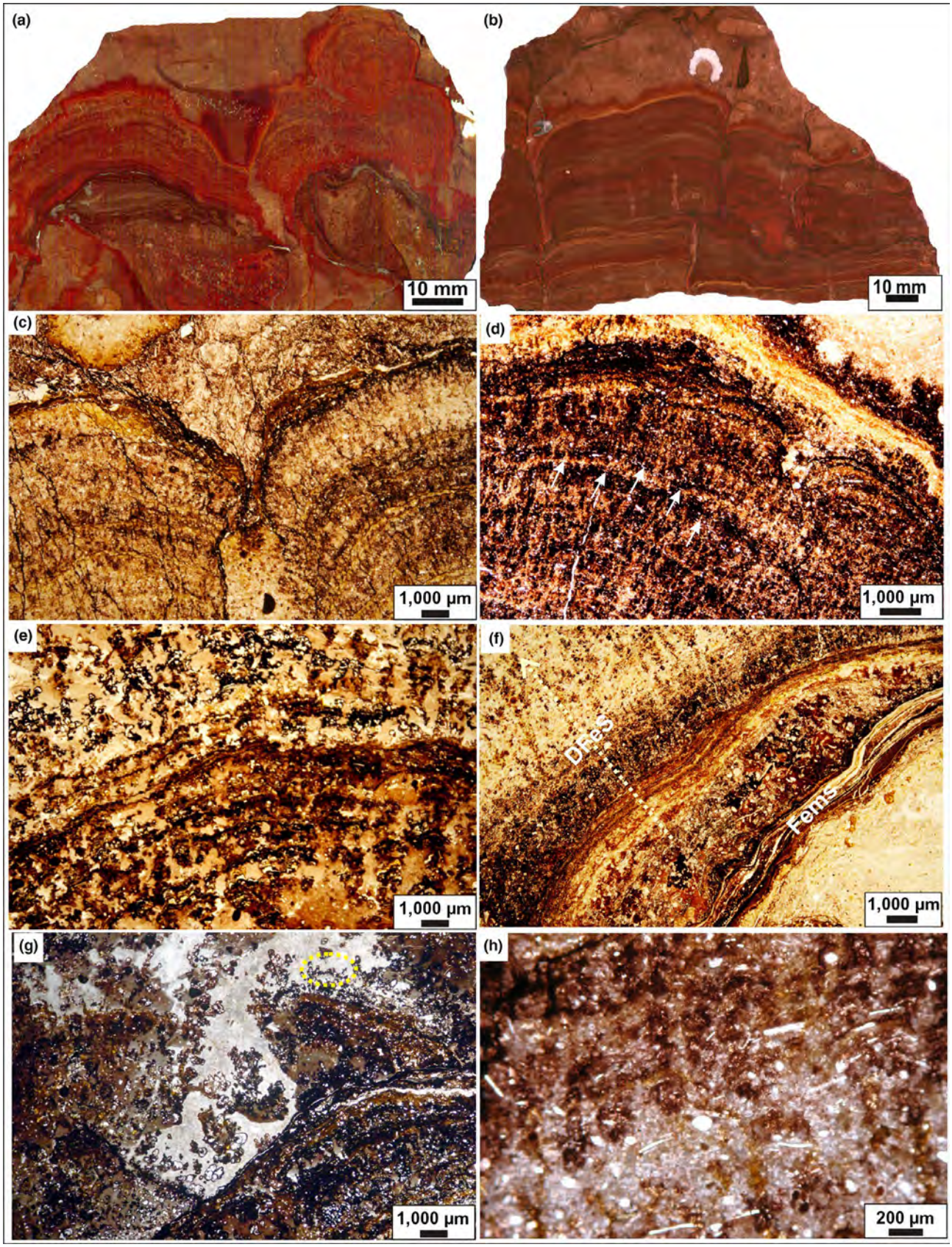

dehydration (Schwertmann & Murad, 1983). In addition, dissimilatory iron-reducing bacteria that can oxidize organic matter and reduce Fe(III) to Fe(II) under anoxic conditions, convert amorphous ferric oxide to magnetite (Lovely, Stolz, Nord, & Phillips, 1987). In all the Fems samples, the XRD analyses revealed that ferriferous component is goethite while hematite and magnetite are the

FIGURE 9 Morphology of the domical ferruginous stromatolites (DFeS): (a, b) polished surfaces showing the domical ferruginous stromatolites forming coalescent clusters; (c–f) The stromatolitic microstructure of DFeS; (d) note the planktonic bivalves shells oriented parallel with thin micritic laminae (white arrows); (e) *Frutexites*-like shrubs developed in between the thin iron-rich micritic laminae; (f) Fems encrusting the hardground surface, followed by DFeS (arrow); between the Fems and DFeS there is a layer of bioclastic wackestone–packstone with planktonic bivalves shells, *Protoglobigerinids* planktonic foraminifera and ostracods; (g) *Frutexites*-like shrubs grow in shelter cavities (pores) generated by the stromatolitic laminae; they are oriented perpendicular on lamination and are fixed on the planktonic bivalves shells (yellow dotted line) or grow from the thin iron-rich micritic laminae; (h) thin irregular wavy or wrinkle laminae of dense iron-rich micrite alternating with thicker micropeloidal laminae or with intercalations of bioclastic wackestone–packstone

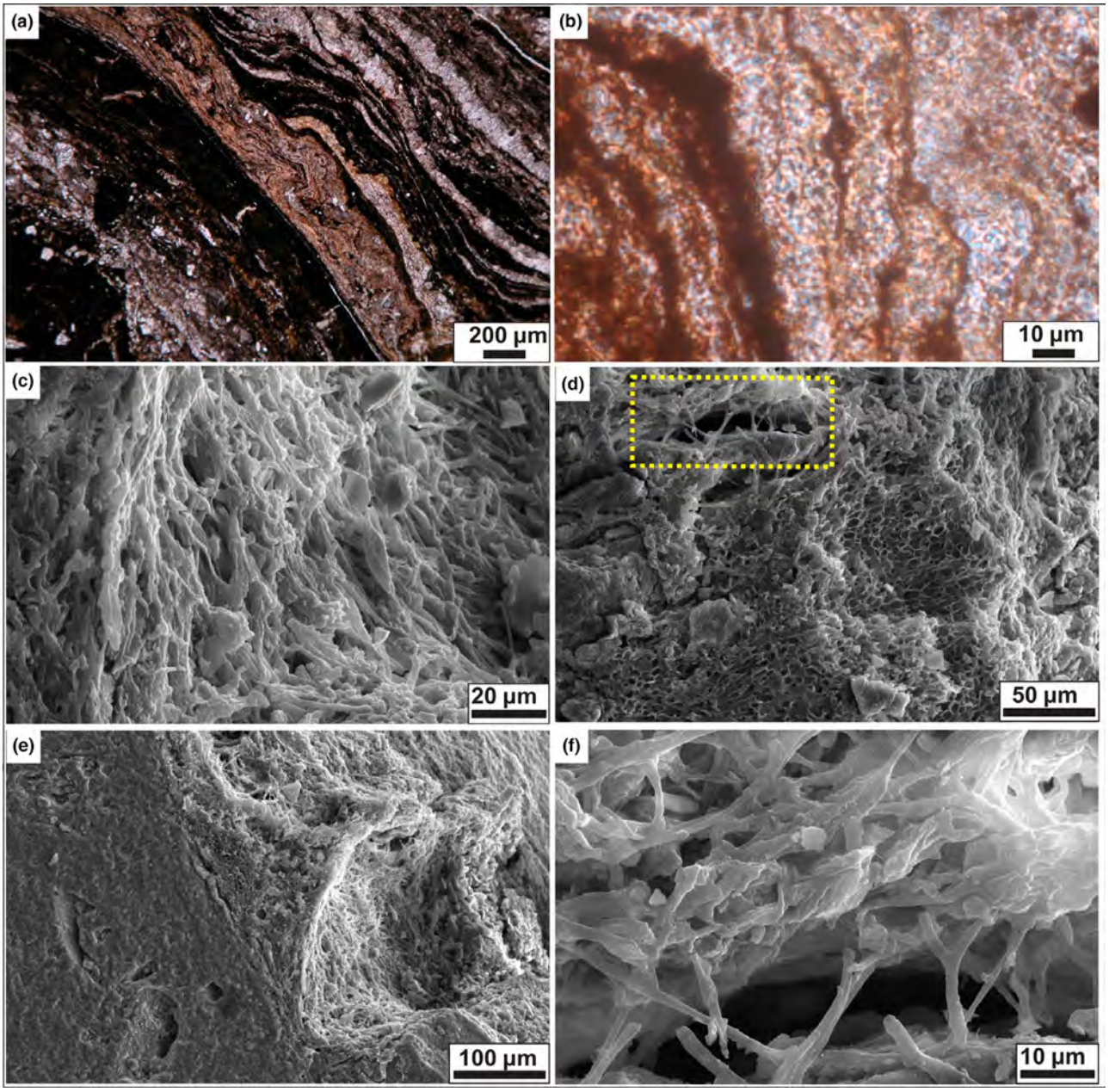

FIGURE 10 Microstructure of the domical ferruginous stromatolites (DFeS): (a, b) thin sections showing the wrinkle morphology of the iron-rich laminae; (b) Note the presence of filaments-like structures forming a dense network within the ferruginous laminae; (c–f) SEM images showing a dense network of filaments-like structures (with a diameter of 1–1.5 µm) with apical dichotomous branching

TABLE 1 X-ray fluorescence analyses (wt. %) of the representative studied ferruginous stromatolites and iron isotopic data

Sample location		Sample ID	SiO_2	TiO_2	Al_2O_3	Fe_2O_3	MnO	MgO	CaO	K_2O	P_2O_5	Total	$\delta^{56}Fe \pm 0.1‰$	$\delta^{57}Fe \pm 0.1‰$
Strunga Pass	Fems	St1	12.54	0.48	5.78	75	0.52	0.01	3.15	0.64	1.88	100	0.18	0.26
		St2	10.93	0.55	6.07	75.37	0.4	0.01	3.32	0.5	2.84	99.99	−0.01	0.00
		St1a	8.06	0.39	3.78	77.27	0.14	0.05	8.64	0.34	1.12	99.79	0.31	0.53
		St2a	7.27	0.28	5.47	73.53	0.19	0.03	11.09	0.29	1.85	100	0.11	0.20
Purcărete Valley		R1	7.89	0.34	6.24	78.79	0.01	0.1	4.72	0.34	1.17	99.6	0.59	0.82
		R2	4.95	0.13	6	77.43	0.05	1.37	9.1	0.25	0.72	100	0.53	0.76
		R3	4.25	0.21	2.5	88.55	0.03	0.42	3.25	0.13	0.66	100	−0.10	−0.14
		R4	12.94	0.39	5.64	68.71	0.33	2.68	7.66	0.67	0.6	99.62	0.50	0.73
		R5	14.92	0.17	6.85	69.42	0.22	3.05	4.1	0.23	0.65	99.61	−0.20	−0.31
		R6	6.31	0.2	2.77	79.88	0.14	0.29	8.94	0.16	0.43	99.12	−0.03	−0.05
		R7	10.16	0.13	8.96	66.25	0.04	3.25	10.49	0.25	0.3	99.83	0.24	0.32
		R8	11.52	0.14	9.27	64.22	0.05	3.9	9.76	0.27	0.35	99.48	0.22	0.31
		R9	9.13	0.1	6.45	70.15	0.25	2.51	10.6	0.23	0.41	99.83	0.48	0.66
Saraorschi Valley		SV7	7.01	0.51	2.37	77.88	0.21	0.04	10.91	0.05	0.84	99.82	0.66	0.96
		SV8	11.3	0.6	5.33	69.18	0.12	0.3	10.08	0.82	1.99	99.72	0.40	0.63
		SV9	12.6	0.19	4.07	71.2	0.1	0.18	10.24	0.41	0.93	99.92	0.46	0.64
	DFeS	SV1	3.61	0.03	2.15	78.05	0.15	0.06	13.73	0.45	0.05	98.28	−0.05	−0.08
		SV2	3.62	0.01	1.13	80.29	0.01	0.12	14.43	0.28	0.02	99.91	−0.63	−0.77
		SV3	2.1	0.25	0.05	80.62	0.25	0.12	16.42	0.16	0.03	100	−0.70	−1.17
		SV4	3.77	0.3	1.24	78.94	0.3	0.06	14.82	0.21	0.25	99.89	−0.75	−1.19
		SV5	2.9	0.15	1.93	70.05	0.35	0.02	24.19	0.3	0.05	99.94	−0.32	−0.49
		SV6	9.53	0.15	0.5	75.77	0.21	0.05	12.5	0.83	0.08	99.62	−0.29	−0.42

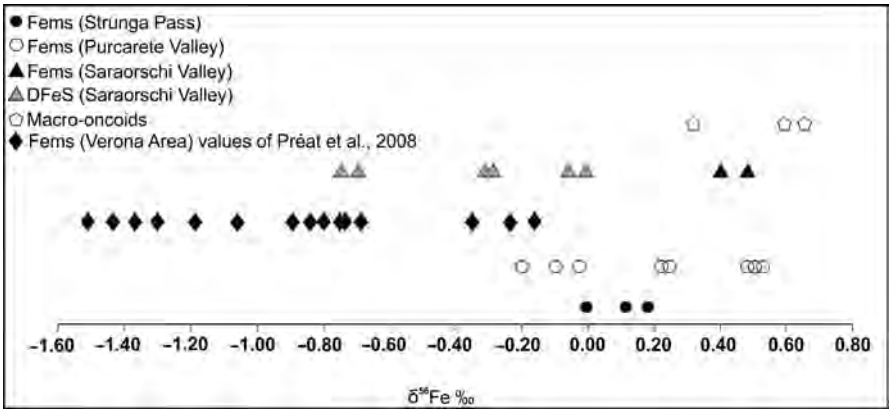

FIGURE 11 Iron isotope composition of the Middle Jurassic ferruginous stromatolites

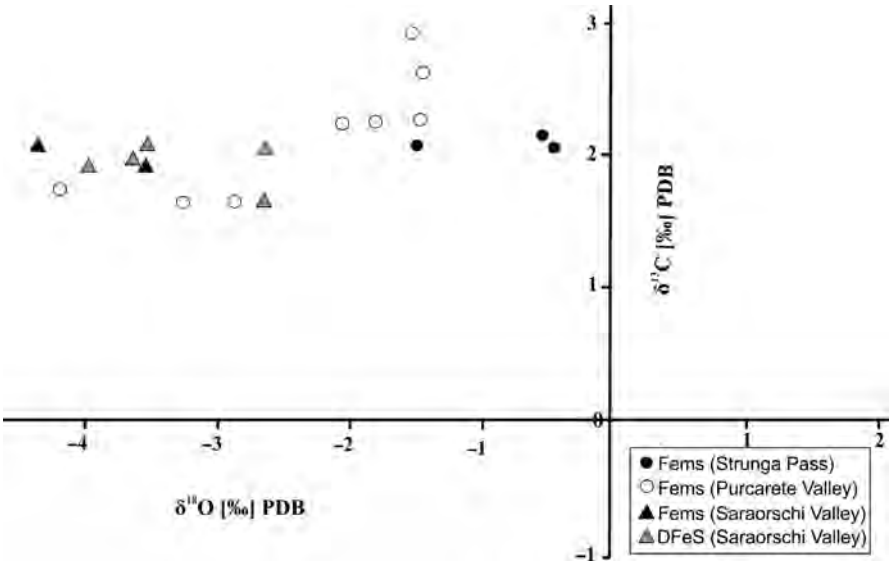

FIGURE 12 Cross-plot of carbon and oxygen isotope values ($\delta^{18}O$ vs. $\delta^{13}C$)

subordinate oxides. The goethite and magnetite might be formed in dysoxic to anoxic conditions as a result of microbial activity capable of coupling Fe(II) oxidation to nitrate reduction (Benz et al., 1998; Chaudhuri, Lack, & Coates, 2001). Alternatively, the XRD analyses performed on the DFeS samples indicate significant amounts of hematite with subordinate quantities of goethite that are associated with iron filaments observed by scanning electron microscopy, which suggests the presence of microbial activity.

5.3 | Paleoenvironmental context of the ferruginous stromatolites formation

5.3.1 | The distribution and behavior of rare-earth elements and yttrium (REE + Y)

The distribution and behavior of rare-earth elements and yttrium (REE + Y) have been widely used as tracers of geochemical processes. The relative abundances of REE + Y in carbonate sediments vary depending on the influence of hydrothermal, terrestrial or marine inputs upon fluids in the basin and of the redox conditions (cf. Allwood, Kamber, Walter, Burch, & Kanik, 2010). More specifically, Eu anomalies reflect the effects of possible hydrothermal input, Y/Ho ratios and La anomalies to identify the terrestrial input on chemical precipitates and to distinguish the marine from terrestrial environment and Ce anomalies are used as redox proxies in marine paleoenvironments (e.g., Alexander, Bau, Andersson, & Dulski, 2008; Bau & Dulski, 1996; Kamber, Bolhar, & Webb, 2004; Webb & Kamber, 2000).

The source of high iron concentrations: In the ferruginous stromatolites studied here, the presence of high iron concentrations, with an average of 74.8% is related of two possible sources: continental weathering and hydrothermal processes.

Continental weathering is an important source of iron and has been suggested for many Phanerozoic iron deposits (Tucker, 1981) and several mechanisms of iron transportation have been proposed. Iron (oxyhydr)oxide often form as colloidal suspensions of gels which are stabilized in the presence of organic matter and can be transported either by rivers and then precipitated in the seawater through coagulation of the colloidal suspensions or iron can be transported by adsorption onto organic matter. Another mechanism is related to iron transport by clay minerals, either as part of the clay structure or as oxide films on the surface of clays. After deposition, the iron can be released from the clays into the pore water, under appropriate

TABLE 2 Carbon and oxygen isotope ratios of the studied ferruginous stromatolites

Location	Samples	δ13C ‰ (PDB)	δ18O ‰ (PDB)
Strunga Pass	St1-Fems	2.08	−1.50
	St2-Fems	2.05	−0.41
	St1a-Fems	2.14	−0.56
Purcărete Valley	R1-Fems	2.22	−2.04
	R2-Fems	2.24	−1.81
	R3-Fems	2.28	−1.49
	R4-Fems	2.95	−1.53
	R5-Fems	2.62	−1.46
	R6-Fems	1.64	−2.86
	R7-Fems	1.76	−4.19
	R8-Fems	1.65	−3.23
Saraorschi Valley	SV1-DFeS	1.93	−3.99
	SV2-DFeS	2.04	−3.52
	SV3-DFeS	2.03	−2.63
	SV4-DFeS	1.96	−3.64
	SV5-DFeS	1.69	−2.64
	SV8-Fems	1.92	−3.53
	SV9-Fems	2.09	−4.34

Eh-pH conditions, and later converted by biologically induced mineralization into crystalline oxyhydroxides as ferrihydrite to goethite and oxides like hematite or magnetite (Tucker, 1981). The oriented clay aggregates analyses reveal that the main mineral phases of the clay fraction are illite and montmorillonite. The SiO_2/Al_2O_3 ratios of the studied samples reflect the presence of clay minerals and other intermixed detrital mineral phases which indicate that one of the sources of iron for the studied ferruginous stromatolites was the continental weathering.

The studied samples show the low LREE/HREE (Pr/Yb (SN) <1) and preferential oxidation/removal of Ce that was interpreted by Planavsky et al. (2010) as values to represent precipitation from seawater which likely reflect lacking significant Mn and Ce cycling due to minimal dissolved O_2 in the water column. On the other hand, the effects of light to heavy REE fractionation and preferential oxidation/removal of Ce in modern and ancient marine systems are represented by the Er/Nd ratio (cf. De Baar, Bacon, Brewer, & Bruland, 1985; German & Elderfield, 1989). The Er/Nd ratio of carbonates reveals the seawater signature with 0.27 ppm for normal seawater and can be reduced up to 0.1 ppm due to preferential concentration of Nd relative to Er when exist an addition of detrital material. The Er/Nd ratio of the Fems from Strunga Pass and Saraorschi Valley is ranging from 0.08 to 0.21 ppm that indicates the contribution of some detrital inputs. This observation is in concordance with mineralogical results obtained which indicate the presence of quartz grains and clay minerals as illite, montmorillonite, kaolinite and chlorite. Furthermore, the $(Dy/Yb)_{SN}$ ratio in all the studied samples have an average of 1.14, being similar to the modern seawater ratio (e.g. ~ 0.8 to 1.2) and the positive La anomalies (with an average of 1.73) are in agreement with deposition in seawaters (e.g. La/La* generally between 1.3 and 1.5).

Some authors have linked the genesis of banded iron formations to hydrothermal fluids released to the deep sea (Derry & Jacobsen, 1990). In this model, the hydrothermal signature was transported into shallow waters by upwelling and then deposited along a chemocline intersecting the basin (Isley, 1995). These arguments suggest that hydrothermal processes could have served as a source of the iron deposited in the formation of the studied ferruginous stromatolites. Under reducing environments, Eu^{3+} is reduced to Eu^{2+} being the only one that may remain in the soluble state in hydrothermal fluids because it is stable at higher temperatures (cf. Bau, 1991). The presence of positive Eu anomaly in many banded iron formations was suggested to be the result of the input from hydrothermal solutions (cf. Bau & Dulski, 1996; Derry & Jacobsen, 1988; Kamber & Webb, 2001). In all the studied ferruginous stromatolites the presence of low positive Eu anomalies (with an average of 1.07) is consistent with reducing conditions and also could be correlated with a diffuse hydrothermal input on the seawater during the accretion of the studied stromatolites. The presence of diffuse hydrothermal input during the Bathonian-Callovian time interval may be documented for the first time in the studied areas and could be related to the opening of the adjacent Ceahlău–Severin Ocean during the Middle-Upper Jurassic interval.

Krepski et al. (2013) described filamentous Fe(III)-oxyhydroxide microfossils from a 170 Ma (Middle Jurassic, Early Bajocian) marine Fe-Si hydrothermal deposit. In the modern oceans, microbial mats of Fe(II) oxidizing micro-organisms are primarily associated with diffuse flow hydrothermal vents (Chan et al., 2016 and references therein).

Cerium is the most abundant REE and has two possible oxidation states, Ce^{3+} and Ce^{4+}. According to Sholkovitz and Schneider (1991) the Ce^{3+} anomaly in seawater is the result of microbial oxidation followed by preferential scavenging of Ce^{4+}. In oxygenated seawater, soluble Ce^{3+} is oxidized to insoluble Ce^{4+} that tends to be rapidly removed by scavenging on the surface of particles such as Fe/Mn (oxyhydr)oxides, organic matter and clay minerals. For this reason, oxygenated seawater is typically depleted in Ce (cf. Elderfield & Greaves, 1982) and shows a strong negative Ce/Ce* anomaly (cf. Webb & Kamber, 2000). In contrast, under suboxic and anoxic conditions, Ce^{+4} is reduced to Ce^{3+}, resulting in minimal fractionation and smaller, absent or positive Ce anomalies due to reductive dissolution of settling iron-rich particles (cf. Byrne & Sholkovitz, 1996; German, Holliday, & Elderfield, 1991; Planavsky et al., 2010; Slack, Grenne, Bekker, Rouxel, & Lindberg, 2007). Positive Ce anomalies and light REE enrichment develop in anoxic and dysoxic waters from some basins, due to reductive dissolution (Bau, Moller, & Dulski, 1997).

The redox cycling of Ce is directed mainly by its selective removal onto Fe-Mn (oxyhydr)oxides. Iron (oxyhydr)oxides record Ce anomalies from the water column from which they precipitated qualitatively, in contrast to Mn oxides that scavenge Ce and LREE preferentially (Bau, 1999). Dysoxic or anoxic waters lead to iron (oxyhydr)

oxide precipitation and positive Ce anomalies would be transferred to the sedimentary record (Planavsky et al., 2010).

The combination of iron oxide enrichment with Ce anomalies, when applied to carbonate sedimentary rocks, can provide important insights into paleoredox conditions (Tostevin et al., 2016).

In the studied samples corresponding to Fems (associated with the hardground surfaces) Ce anomalies display moderate negative value in the Purcărete Valley and small negative Ce anomalies in Strunga Pass and Saraorschi Valley, respectively. In the Fems samples that form the cortex of the macro-oncoids from all the studied sections, Ce anomalies indicate large to small negative values, showing fluctuation in oxygenated conditions. In the Purcărete Valley, the presence of moderately negative Ce anomalies related to Fems samples, show that oxidized phases alternate with poorly oxygenated conditions in specific micro-environments, located in an open-marine offshore transition depositional environment, results that are in agreement with those obtained in previous studies (Lazăr & Grădinaru, 2014). Moderate to very small negative Ce anomalies obtained in the Strunga Pass samples reflect the formation of Fems under weakly oxygenated conditions, in slowly reducing environment that is in concordance with the results achieved by Lazăr et al. (2013). These authors inferred a depositional setting corresponding to open-marine environments, below fair-weather wave-base or near to storm wave-base, within the deep euphotic/dysphotic zone. These environments were characterized by low sedimentation rates and early marine cementation, intervals of omission/ non-deposition, erosion and in situ reworking, produced by bottom currents and storm events, generating dysoxic/anoxic interfaces (Lazăr et al., 2013). In the Saraorschi Valley, the Fems samples present small negative Ce anomalies being consistent with the formation under poorly oxygenated environment. Conversely, the DFeS developed at the base of *Ammonitico Rosso*-type limestones, show moderate positive Ce anomalies suggesting that these stromatolites were formed in deeper at the anoxic–suboxic interfaces. The *Ammonitico Rosso*-type limestones containing the DFeS suggest a transition from deep-subtidal to hemipelagic environments, corresponding to a submarine plateau characterized by absence of light, scarcity of oxygen (indicated also by weak bioturbation), low sedimentation rate (indicated by ferruginous hardgrounds; cf. Préat et al., 2011; Préat, Morano, Loreau, Durlet, & Mamet, 2006 and references therein).

Yttrium has similar chemical properties to the REEs and it is considered analogous to holmium (Ho) because they both have identical ionic radii and valences, respectively (cf. Bau & Dulski, 1995). Yttrium, which is less particle reactive than Ho (Bau et al., 1997; Planavsky et al., 2010), has a distinct behavior in aqueous solutions (Nozaki, Zhang, & Amakawa, 1997). The presence of positive Y anomalies (resulting in Y/Ho ratios) is common for marine seawaters with higher Y anomalies (~40–80) occurring in open-marine settings and smaller Y anomalies (~33–40) in near shore or restricted settings whereas terrigenous materials and volcanic ash have constant Y/Ho ratios of ~28 (Bau et al., 1997; Tostevin et al., 2016).

In the studied samples, the Y/Ho ratio is closer to those of seawater (~40–80), being variable with an average of 52.55 in Strunga Pass, 35.85 in Purcărete Valley and 35.80 in Saraorschi Valley, indicating that these ratios were influenced by REE + Y scavenging during iron (oxyhydr)oxide precipitation in ferruginous stromatolites. The low Y/Ho ratios in all the studied samples suggest a detrital input influenced by high siliciclastic components represented by quartz grains. Generally, the Y anomaly is less pronounced in samples with high iron concentration and higher clay minerals (Tostevin et al., 2016).

5.3.2 | Stratigraphic records of the stable isotope composition of $\delta^{13}C$

Stratigraphic records of the stable isotope composition of $\delta^{13}C$ have been widely used as proxies for paleoenvironmental reconstruction (cf. Veizer et al., 1999). The carbon isotope ratios of ferruginous stromatolites are useful for the reconstruction of ancient environmental changes whereas the oxygen isotope ratios are mainly used here to constrain the diagenetic processes. Most of the carbonates that precipitate from seawater have an equilibrium isotopic composition, with low positive $\delta^{13}C$ and low negative $\delta^{18}O$ values (Marshall & Ashton, 1980; Veizer et al., 1999). The studied ferruginous stromatolites (Fems and DFeS) from all the studied sections have normal marine $\delta^{13}C$ values varying between 1.64‰ and 2.95‰. These values are consistent with precipitation in equilibrium with marine waters (cf. Marshall & Ashton, 1980; Veizer et al., 1999). The oxygen isotopic composition is depleted in $\delta^{18}O$ in all the studied samples, with values from −0.41‰ to −4.34‰. Oxygen isotopes of carbonate rocks become progressively more depleted in $\delta^{18}O$ either due to elevated temperature, the alteration of the original isotopic compositions or with increasing age of the rocks (Veizer et al., 1999). However, the samples from Saraorschi Valley have the lowest $\delta^{18}O$ values (from −2.64‰ to −4.34‰), suggesting that these samples were apparently slightly affected by thermal overprint during the burial diagenesis.

5.3.3 | Total organic carbon (TOC) contents

Total organic carbon (TOC) contents of the studied ferruginous stromatolites samples range from 0.22% to 2.62% as a result of the low preservation of organic matter content due to its degradation which could have been influenced by redox oscillations. Significant differences in the TOC concentrations of the analyzed stromatolites samples are also reflected in the calcium carbonate content. The Fems present the overall highest TOC values (~2.18%) and an average of 3% carbonate content. Variations of the generally high calcium carbonate content with an average of 58.28% and very low TOC content (~0.39%) of DFeS samples mostly reflect fluctuations in the ratio of biogenic iron-rich carbonate to terrigenous sediment inputs such as illite and montmorillonite.

TABLE 3 Rare earth element (REE-Y) concentrations (in ppm) in the studied ferruginous stromatolites

Sample location	Fems										
	Strunga Pass				Purcărete Valley						
Sample ID	St1	St2	St1a	St2a	R1	R2	R3	R4	R5	R6	R7
La	3.4	2.69	2.81	3.6	9	8.29	11.20	21.18	8.62	5.90	6.97
Ce	4.36	4.74	3.97	6.46	5.61	5.87	15.05	28.13	10.46	6.95	8.44
Pr	0.55	0.48	0.46	0.66	1.21	1.15	2.89	4.01	2.45	1.55	1.90
Nd	2.33	2.05	1.95	2.77	5.17	4.91	13.27	17.10	11.52	7.33	8.93
Sm	0.46	0.47	0.4	0.63	1.19	1.15	3.79	4.16	3.38	2.03	2.54
Eu	0.11	0.11	0.09	0.15	0.3	0.29	1.06	1.08	0.91	0.55	0.69
Gd	0.55	0.56	0.48	0.74	1.6	1.55	5.20	5.30	4.32	2.71	3.36
Tb	0.09	0.1	0.08	0.13	0.28	0.28	0.98	0.99	0.80	0.48	0.62
Dy	0.54	0.62	0.49	0.82	1.89	1.88	6.59	6.57	5.25	3.16	4.03
Y	6.81	7.22	5.97	8.57	20.21	18.51	50.80	45.89	34.76	23.83	27.65
Ho	0.12	0.14	0.11	0.18	0.44	0.43	1.43	1.43	1.14	0.70	0.88
Er	0.36	0.43	0.35	0.55	1.43	1.4	4.08	4.19	3.33	2.04	2.61
Tm	0.05	0.06	0.05	0.08	0.22	0.22	0.51	0.56	0.46	0.27	0.36
Yb	0.33	0.43	0.39	0.53	1.63	1.59	2.97	3.61	3.00	1.70	2.30
Lu	0.05	0.06	0.06	0.07	0.24	0.23	0.40	0.50	0.42	0.24	0.32
Σ REE	20.11	20.16	17.66	25.94	50.42	47.75	120.22	144.69	90.82	59.44	71.61
Ce/Ce*	0.72	0.95	0.79	0.96	0.38	0.42	0.61	0.70	0.52	0.53	0.53
Eu/Eu*	1.09	1.03	1.02	1.06	1.06	1.05	1.12	1.09	1.13	1.15	1.13
Y/Y*	2.12	1.91	1.91	1.83	1.94	1.83	2.76	2.60	2.25	1.94	2.01
$(La/Yb)_{SN}$	0.76	0.46	0.53	0.50	0.41	0.38	0.28	0.43	0.21	0.25	0.22
$(La/Nd)_{SN}$	1.29	1.16	1.28	1.15	1.54	1.50	0.75	1.10	1.04	0.71	0.69
$(Nd/Yb)_{SN}$	0.59	0.40	0.42	0.43	0.26	0.26	0.37	0.39	0.32	0.36	0.32
$(Dy/Yb)_{SN}$	0.99	0.87	0.76	0.93	0.7	0.71	1.34	1.10	1.05	1.12	1.06
$(Pr/Yb)_{SN}$	0.53	0.36	0.38	0.40	0.24	0.23	0.31	0.35	0.26	0.29	0.26
$(Sm/Yb)_{SN}$	0.71	0.55	0.52	0.60	0.37	0.37	0.65	0.58	0.57	0.60	0.56
Er/Nd	0.15	0.21	0.18	0.20	0.28	0.28	0.31	0.24	0.29	0.28	0.29
Pr/Pr*	1.10	0.91	0.97	0.92	1.23	1.19	1.13	1.06	1.18	1.16	1.17
La/La*	1.80	1.67	1.78	1.55	2.22	2.15	1.46	1.56	1.48	1.64	1.53
Y/Ho	56.75	51.57	54.27	47.61	45.93	43.05	35.43	32.10	30.61	34.28	31.28

Note: All REE-Y concentrations were normalized to post-Archean Australian Shale (PAAS, cf. Taylor and McLennan, 1985).

5.3.4 | Iron isotope ratios provide insights into biogeochemical processes

In modern and ancient environments, iron isotope fractionation can occur upon transformation of iron redox species (between aqueous ferrous and ferric species) and may reflect a combination of kinetic and equilibrium fractionations during rapid dissolution and precipitation (cf. Frierdich, Beard, Reddy, Scherer, & Johnson, 2014; Welch, Beard, Johnson, & Braterman, 2003).

The biologically induced iron mineralization processes that form diverse ferruginous stromatolites include microbial oxidation of ferrous iron (Fe(II)) to ferric iron (Fe(III)), at near-neutral pH at the dysoxic–anoxic interfaces (cf. Planavsky et al., 2009).

Iron isotope analysis performed on ferruginous stromatolites and banded iron formations have been widely used to support the interpreted activity of iron-oxidizing bacteria (e.g., Czaja et al., 2013; Czaja, Kranendonkc, Beard, & Johnson, 2018; Konhauser, Kappler, & Roden, 2011). Positive iron isotope fractionation occurs during redox changes and is connected with the partial oxidation of dissolved ferrous iron (Dauphas, Cates, Mojzsis, & Busigny, 2007; Heimann et al., 2010; Johnson, Beard, Klein, Beukes, & Roden, 2008; Rouxel, Bekker, & Edwards, 2005). It has been shown that partial oxidation of ferrous iron to ferric iron precipitate either through abiotic (e.g., Bullen, White, Childs, Vivit, & Schulz, 2001) or biogenic process at circumneutral pH (cf. Beard et al., 1999). The δ^{56}Fe values of the Fems samples show low negative to positive values (from

					DFeS					
		Saraorschi Valley			Saraorschi Valley					
R8	R9	SV7	SV8	SV9	SV1	SV2	SV3	SV4	SV5	SV6
11.59	13.25	8.32	5.36	10.35	13.99	24.43	20.87	19.38	23.14	22.85
14.99	13.85	11.77	8.04	16.08	38.49	44.67	45.19	46.76	44.1	49.14
3.22	2.49	1.53	0.88	2.09	2.05	4.05	3.82	3.61	4.01	4.23
15.11	10.53	6.52	3.71	8.94	9.18	17.33	16.9	16.58	17.01	18.43
4.33	2.31	1.41	0.77	1.97	1.9	3.84	4.81	4.02	3.45	4.29
1.20	0.57	0.35	0.42	0.41	0.45	0.88	0.78	0.96	0.67	0.96
5.86	2.97	1.52	0.9	2.11	2.2	4.39	4.72	4.69	3.59	4.82
1.09	0.49	0.24	0.15	0.34	0.34	0.64	0.81	0.76	0.51	0.76
7.25	3.05	1.42	0.94	1.95	1.9	3.47	4.04	4.23	2.66	4.09
53.77	23.78	11.16	7.86	14.39	15.5	26.84	21.3	24.98	19.32	24.14
1.59	0.66	0.3	0.19	0.4	0.39	0.68	0.76	0.8	0.51	0.77
4.63	1.89	0.89	0.58	1.2	1.06	1.81	2.15	2.05	1.33	1.99
0.61	0.26	0.13	0.09	0.18	0.14	0.22	0.22	0.24	0.16	0.24
3.69	1.68	0.96	0.6	1.31	0.87	1.43	1.4	1.45	1.01	1.45
0.51	0.23	0.14	0.09	0.2	0.13	0.21	0.28	0.2	0.14	0.2
129.44	78.02	46.66	30.58	61.92	88.59	134.89	128.05	130.71	121.61	138.36
0.56	0.55	0.76	0.84	0.80	1.62	1.02	1.16	1.28	1.04	1.15
1.13	1.09	1.20	1.19	1.00	1.12	1.11	0.79	1.11	0.99	1.06
2.83	1.99	1.63	1.62	1.67	1.94	2.25	1.81	2.09	2.05	2.06
0.23	0.58	0.64	0.66	0.58	1.19	1.26	1.10	0.99	1.69	1.16
0.68	1.12	1.13	1.28	1.03	1.35	1.25	1.10	1.04	1.21	1.10
0.34	0.52	0.56	0.51	0.57	0.88	1.01	1.00	0.95	1.40	1.06
1.18	1.09	0.89	0.94	0.90	1.32	1.46	1.74	1.76	1.59	1.70
0.28	0.47	0.51	0.47	0.51	0.75	0.90	0.87	0.79	1.27	0.93
0.60	0.70	0.75	0.65	0.76	1.11	1.36	1.75	1.41	1.74	1.50
0.31	0.18	0.14	0.16	0.13	0.11	0.10	0.13	0.12	0.08	0.11
1.15	1.16	1.02	0.95	1.02	0.62	0.85	0.81	0.76	0.86	0.82
1.50	1.54	1.61	1.75	1.48	2.36	1.81	1.82	2.04	1.69	1.71
33.90	36.15	37.20	41.37	35.98	39.74	39.47	28.03	31.23	37.88	31.35

−0.20‰ to + 0.66‰) with predominantly positive values indicating the prevalence of partial ferrous iron oxidation maintained by the iron-oxidizing bacteria in the early depositional process. Partial oxidation is necessary for the expression of the iron oxide Fe isotope fractionation and requires dysoxic or anoxic conditions (Planavsky et al., 2009) which mean that the δ^{56}Fe data of the Fems are likely influenced by the extent of oxidation. DFeS samples from Saraorschi Valley exhibit variably low negative δ^{56}Fe compositions (ranging from −0.05‰ to −0.75‰). There are several hypotheses that could explain this depletion of heavy iron isotopes and could have contributed to the origin of ferruginous stromatolites with negative δ^{56}Fe values: dilution of the iron isotope composition of Fe(II) in seawater in connection with various oceanic iron sources such as riverine detritus, atmospheric input, sediment pore waters, and hydrothermal sources (Anbar & Rouxel, 2007; Planavsky et al., 2009; Rouxel, Shanks, Bach, & Edwards, 2008). The light iron isotope is presumably sourced from hydrothermal systems, with the dissolved iron partial oxidation during transport from hydrothermal to shallower depositional environment (von Blanckenburg, Marnberti, Schoenberg, Kamber, & Webb, 2008; Planavsky et al., 2010). The iron isotope composition of hydrothermal fluids varies and several studies report a range from −0.09‰ to −0.67‰ (Beard et al., 2003, Rouxel et al., 2008; Severmann et al., 2004).

Additionally, extensive microbial dissimilatory iron reduction by Fe(III) reducing bacteria in dysoxic to anoxic conditions also appear to be characterized by negative δ^{56}Fe values (Beard et al., 1999; Préat

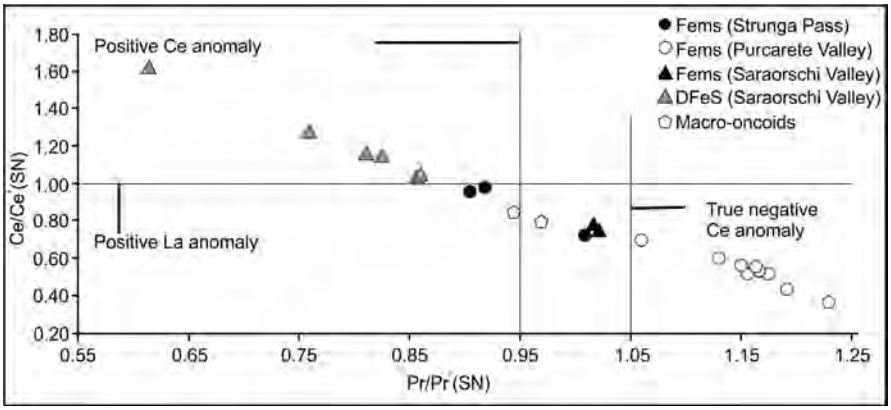

FIGURE 13 Plot of post-Archean Australian shale (PAAS)-normalized $Pr/Pr^{*} = Pr_{SN}/(0.5Ce_{SN} + 0.5Nd_{SN})$ versus $(Ce/Ce^{*} = Ce_{SN}/(0.5La_{SN} + 0.5Pr_{SN})$. The plot discriminates between positive La and true negative Ce anomalies on the studied samples

et al., 2008; Severmann, Johnson, Beard, & McManus, 2006). In the studied ferruginous stromatolites, the lowest δ^{56}Fe values may indicate a possible biofractionation, that probably depend on changes in microenvironmental conditions (Eh, pH, low oxygen content) as well as various iron sources. The presence of well-preserved filamentous bodies coated with iron (oxyhydr)oxide (Figure 10) indicates that the lower δ^{56}Fe values in the ferruginous stromatolites could then be interpreted as reflecting a possible biogenic iron (oxyhydr)oxide formation. The iron bacteria have precipitated iron (oxyhydr)oxide (subsequently transformed in hematite and goethite) with preferentially lower iron isotopes in their tubular structures. Our results are in concordance with those of Préat et al. (2008) who documented that the iron oxides have formed in close association with bacteria and fungi and which have recorded a low negative Fe isotopic value (with an average δ^{56}Fe value of −0.84‰, Figure 11). In conclusion, iron isotope compositions of microbial laminae from all the studied ferruginous stromatolites display a range between −0.75‰ and +0.66‰ which indicate that iron isotope compositions of hydrothermal iron (oxyhydr)oxide precipitates are sensitive to local environmental conditions where they form. Rouxel, Toner, Germain, and Glazer (2018) proposed that both positive and negative δ^{56}Fe values are likely the result of partial oxidation of iron formation near or below the seafloor during the circulation of low-temperature hydrothermal source.

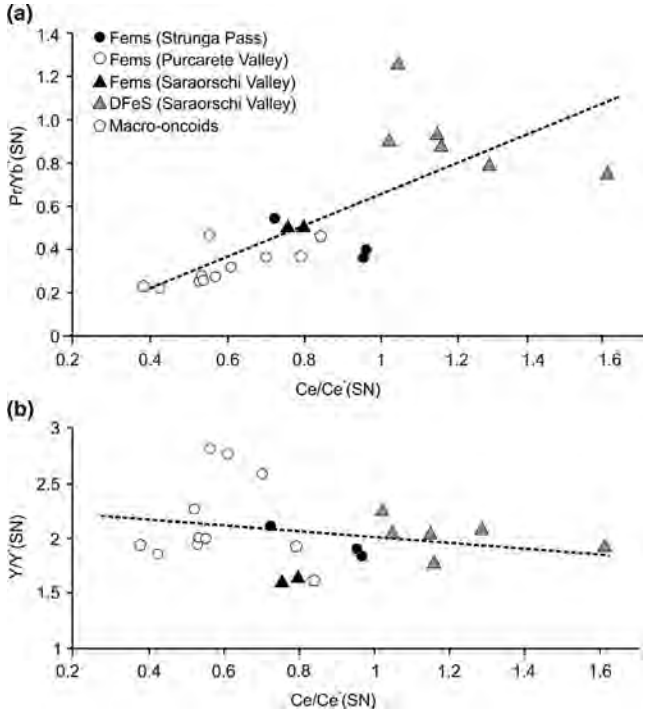

FIGURE 14 Cross-plots of REE + Y characteristics of the studied ferruginous stromatolites. (a) Light to heavy REE ratios calculated as the Pr_{SN}/Yb_{SN} ratio versus Ce anomalies. (b) Y_{SN}/Y_{SN} ratio versus Ce anomalies $(Ce_{SN}/(0.5(Pr_{SN} + La_{SN})$

6 | CONCLUSIONS

Based on the morphological and geochemical results, we propose that microaerophilic Fe-oxidizing micro-organisms played a significant role in the genesis of the Middle Jurassic (Bathonian–Callovian) ferruginous stromatolites. The narrow range of widths, the biogenic branching patterns and the directional orientation of the filamentous structures observed within the iron-rich laminae, are consistent with the data previously obtains for recent microaerophilic Fe-oxidizing micro-organisms.

Considering the microfossils observed in Fems laminae and the iron isotopes data predominantly positive, near zero, or even low negative values (from −0.20‰ to +0.66‰), we infer that there was partial oxidation of Fe(II) to Fe(III) precipitation maintained by the Fe(II)-oxidizing bacteria. These data are consistent with moderate to small negative Ce anomalies indicating weakly oxygenated conditions suitable with slowly reducing environments at the site of the formation of Fems.

The lowest negative δ^{56}Fe values (up to −0.75‰) present only in DFeS samples point to initial iron mobilization where the Fe(II) was produced by dissimilatory Fe(III) reduction of ferric oxides by Fe(III)-reducing bacteria. These data are in agreement with moderate positive Ce anomalies suggesting that they formed in deeper environments, at anoxic–suboxic waters–sediment interfaces.

In all the ferruginous stromatolites, the presence of high iron concentrations with an average of 74.8% is related of two possible sources: continental weathering and hydrothermal processes. The continental weathering is suggested by the presence of clay fraction

represented by illite, montmorillonite, and Er/Nd ratio ranging from 0.08 to 0.21 ppm.

The presence of positive Eu anomalies (with an average of 1.07) and the negative iron isotope values show that local development of the DFeS could be related to diffuse hydrothermal input on the sites of their formation.

ACKNOWLEDGMENTS

This research was supported by the Research Institute of the University of Bucharest (ICUB) project for Young Researchers, 28544/2017. We thank our colleagues Mihai E. Popa (University of Bucharest) and Emanoil Săsăran (Babes-Bolyai University, Cluj-Napoca) for using their microscopy equipment. We are grateful to the reviewers Maxwell Lechte and Alain R. Préat and to the editor N. J. Planavsky for their corrections, comments, and suggestions that strongly improved the original manuscript.

AUTHOR CONTRIBUTIONS

M.G. and I.L. conducted the design, field work, prepared samples, thin sections, polished slabs, light micrographs, and acquired ESEM/EDS data, performed XRF and CL analyses, microfacies analyses and wrote the paper. M.G. and M.N.D. performed REE + Y and iron isotopes measurements. L.P. acquired XRD data.

ORCID

Mihaela Grădinaru https://orcid.org/0000-0003-3669-0472

REFERENCES

Abad, I., & Reolid, M. (2012). Hydrothermal and hydrogenetic origins of the Middle Jurassic Fe and Mn crusts from Betic-Rifian Cordillera based on geochemical analyses. *Revista De La Sociedad Española De Mineralogía*, *16*, 224–225.

Alexander, B. W., Bau, M., Andersson, P., & Dulski, P. (2008). Continentally-derived solutes in shallow Archean seawater: Rare earth element and Nd isotope evidence in iron formation from the 2.9Ga Pongola Supergroup, South Africa. *Geochimica Et Cosmochimica Acta*, *72*, 378–394. https://doi.org/10.1016/j.gca.2007.10.028

Allwood, A. C., Kamber, B. S., Walter, M. R., Burch, I. W., & Kanik, I. (2010). Trace elements record depositional history of an Early Archean stromatolitic carbonate platform. *Chemical Geology*, *270*, 148–163. https://doi.org/10.1016/j.chemgeo.2009.11.013

Anbar, A. D., & Rouxel, O. (2007). Metal stable isotopes in paleoceanography. *Annual Review of Earth and Planetary Sciences*, *35*, 717–746. https://doi.org/10.1146/annurev.earth.34.031405.125029

Arnold, G. L., Weyer, S., & Anbar, A. D. (2004). Fe isotope variations in natural materials measured using high mass resolution multiple collector ICPMS. *Analytical Chemistry*, *76*, 322–327. https://doi.org/10.1021/ac034601v

Awramik, S. M., & Baghoorn, E. S. (1977). The Gunflint microbiota. *Precambrian Research*, *5*, 121–142. https://doi.org/10.1016/0301-9268(77)90025-0

Balintoni, I., Balica, C., Ducea, M. N., & Hann, H. P. (2014). Peri-Gondwanan terranes in the Romanian Carpathians: A review of their spatial distribution, origin, provenance and evolution. *Geoscience Frontiers*, *5*, 395–411. https://doi.org/10.1016/j.gsf.2013.09.002

Bau, M. (1991). Rare-earth element mobility during hydrothermal and metamorphic fluid-rock interaction and the significance of the oxidation state of europium. *Chemical Geology*, *93*, 219–230. https://doi.org/10.1016/0009-2541(91)90115-8

Bau, M. (1999). Scavenging of dissolved yttrium and rare earths by precipitating iron oxyhydroxide: Experimental evidence for Ce oxidation, Y-Ho fractionation, and lanthanide tetrad effect. *Geochimica Et Cosmochimica Acta*, *63*, 67–77. https://doi.org/10.1016/S0016-7037(99)00014-9

Bau, M., & Dulski, P. (1995). Comparative study of yttrium and rare-earth element behaviours in fluorine-rich hydrothermal fluids. *Contributions to Mineralogy and Petrology*, *119*, 213–223. https://doi.org/10.1007/BF00307282

Bau, M., & Dulski, P. (1996). Distribution of yttrium and rare-earth elements in the Penge and Kuruman iron-formations, Transvaal Supergroup, South Africa. *Precambrian Research*, *79*, 37–55. https://doi.org/10.1016/0301-9268(95)00087-9

Bau, M., Moller, P., & Dulski, P. (1997). Yttrium and lanthanides in eastern Mediterranean seawater and their fractionation during redox-cycling. *Marine Chemistry*, *56*, 123–131. https://doi.org/10.1016/S0304-4203(96)00091-6

Beard, B. L., Johnson, C. M., Cocs, L., Sun, H., Nealson, K. H., & Aguilar, C. (1999). Iron isotope biosignatures. *Science*, *285*, 1889–1892. https://doi.org/10.1126/science.285.5435.1889

Beccaro, P., & Lazăr, I. (2007). Oxfordian and Callovian radiolarians from the Bucegi Massif and Piatra Craiului Mountains (Southern Carpathians, Romania). *Geologica Carpathica*, *58*(4), 305–320.

Benz, M., Brune, A., & Schink, B. (1998). Anaerobic and aerobic oxidation of ferrous iron at neutral pH by chemoheterotrophic nitrate-reducing bacteria. *Archives of Microbiology*, *169*, 159–165. https://doi.org/10.1007/s002030050555

Böhm, F., & Brachert, T. C. (1993). Deep-water stromatolites and Frutexites Maslov from the Early and Middle Jurassic of S-Germany and Austria. *Facies*, *28*, 145–168. https://doi.org/10.1007/BF02539734

Bullen, T. D., White, A. F., Childs, C. W., Vivit, D. V., & Schulz, M. S. (2001). Demonstration of significant abiotic iron isotope fractionation in nature. *Geology*, *29*, 699–702. https://doi.org/10.1130/0091-7613(2001)029<0699:DOSAII>2.0.CO;2

Burkhalter, R. M. (1995). Ooidal ironstones and ferruginous microbialites: Origin and relation to sequence stratigraphy (Aalenian and Bajocian, Swiss Jura mountains). *Sedimentology*, *42*, 57–74. https://doi.org/10.1111/j.1365-3091.1995.tb01271.x

Byrne, R. H., & Sholkovitz, E. R. (1996). Marine chemistry and geochemistry of the lanthanides. In K. A. Gschneider, Jr., & E. LeRoy (Eds.), *Handbook on the Physics and Chemistry of Rare Earths* (vol. *23*, pp. 497–593). Amsterdam, Netherlands: Elsevier.

Callomon, J. H., & Grădinaru, E. (2005). From the thesaurus of the museum collections. I. Liassic ammonites from Munteana (Sviniţa zone, Southern Carpathians, Romania). *Acta Paleontologica Romaniae*, *5*, 49–65.

Chan, C. S., Emerson, D., & Luther, G. W. (2016). The role of microaerophilic Fe-oxidizing micro-organisms in producing banded iron formations. *Geobiology*, *14*, 509–528. https://doi.org/10.1111/gbi.12192

Chaudhuri, S. K., Lack, J. G., & Coates, J. D. (2001). Biogenic magnetite formation through anaerobic bio-oxidation of Fe(II). *Applied and Environmental Microbiology*, *67*, 2844–2848. https://doi.org/10.1128/AEM.67.6.2844-2848.2001

Codarcea, A., Răileanu, G. R., Liteanu, E., Savu, H., Ghenea, C., & Ghenea, A. (1966). Geological Map of Romania, Sheet 40 Turnu-Severin L-34-XXXV, map scale 1:200000, Geological Institute of Romania.

Czaja, A. D., Johnson, C. M., Beard, B. L., Roden, E. E., Li, W., & Moorbath, S. (2013). Biological Fe oxidation controlled deposition of banded iron formation in the ca. 3,770 Ma Isua Supracrustal Belt (West Greenland). *Earth and Planetary Science Letters*, *363*, 192–203. https://doi.org/10.1016/j.epsl.2012.12.025

Czaja, A. D., Van Kranendonkc, M. J., Beard, B. L., & Johnson, C. M. (2018). A multistage origin for Neoarchean layered hematite-magnetite iron formation from the Weld Range, Yilgarn Craton, Western Australia. *Chemical Geology*, *488*, 125–137. https://doi.org/10.1016/j.chemgeo.2018.04.019

Dauphas, N., Cates, N. L., Mojzsis, S. J., & Busigny, V. (2007). Identification of chemical sedimentary protoliths using iron isotopes in the N3750 Ma Nuvvuagittuq supracrustal belt, Canada. *Earth and Planetary Science Letters*, *254*, 358–376.

De Baar, H. J. W., Bacon, M. P., Brewer, P. G., & Bruland, K. W. (1985). Rare earth elements in the Atlantic and Pacific Oceans. *Geochimica Et Cosmochimica Acta*, *49*, 1943–1959.

Derry, L. A., & Jacobsen, S. B. (1988). The Nd and Sr evolution of Proterozoic seawater. *Geophysical Research Letters*, *15*, 397–400.

Derry, L. A., & Jacobsen, S. B. (1990). The chemical evolution of Precambrian seawater: Evidence from REEs in banded iron formations. *Geochimica Cosmochimica Acta*, *54*, 2965–2977. https://doi.org/10.1016/0016-7037(90)90114-Z

Ducea, M. N., Negulescu, E., Profeta, L., Săbău, G., Jianu, D., Petrescu, L., & Hoffman, D. (2016). Evolution of the Sibişel Shear Zone (South Carpathians): A study of its type locality near Răşinari (Romania) and tectonic implications. *Tectonics*, *35*, 1–27. https://doi.org/10.1002/2016TC004193

Elderfield, H., & Greaves, M. J. (1982). The rare earth elements in seawater. *Nature*, *296*, 214–219. https://doi.org/10.1038/296214a0

Frierdich, A. J., Beard, B. L., Reddy, T. R., Scherer, M. M., & Johnson, C. M. (2014). Iron isotope fractionation between aqueous Fe(II) and goethite revisited: New insights based on a multi-direction approach to equilibrium and isotopic exchange rate modification. *Geochimica Et Cosmochimica Acta*, *139*, 383–398. https://doi.org/10.1016/j.gca.2014.05.001

Fürsich, F. T. (1978). The influence of faunal condensation and mixing on the preservation of fossil benthic communities. *Lethaia*, *11*(3), 243–250. https://doi.org/10.1111/j.1502-3931.1978.tb01231.x

Galácz, A. (1994). Ammonite stratigraphy of the Bathonian red, nodular marl in the Mecsek Mts (S Hungary). *Annales Universitatis Scientiarum Budapestinensis De Rolando Eötvös Nominatae*, *Sectio Geologica*, *30*, 115–150.

German, C. R., & Elderfield, H. (1989). Rare earth elements in Saanich Inlet, British Columbia, a seasonally anoxic basin. *Geochimica Et Cosmochimica Acta*, *53*, 2561–2571. https://doi.org/10.1016/0016-7037(89)90128-2

German, C. R., Holliday, B. P., & Elderfield, H. (1991). Redox cycling of rare earth elements in the suboxic zone of the Black Sea. *Geochimica Et Cosmochimica Acta*, *55*, 3553–3558. https://doi.org/10.1016/0016-7037(91)90055-A

Gómez, J. J., & Fernández-López, S. (1994). Condensation processes in shallow platforms. *Sedimentary Geology*, *92*, 147–159. https://doi.org/10.1016/0037-0738(94)90103-1

Grădinaru, M. (2011). Geneza hardground-urilor jurasice din Munţii Bucegi (versantul vestic) şi din Munţii Almăjului (Sviniţa). Unpublished PhD thesis, University of Bucharest.

Gradziński, M., Tyszka, J., Uchman, A., & Jach, R. (2004). Large microbial foraminiferal oncoids from condensed Lower-Middle Jurassic deposits: A case study from the Tatra Mountains, Poland. *Palaeogeography, Palaeoclimatology, Palaeoecology*, *213*, 133–151. https://doi.org/10.1016/j.palaeo.2004.07.010

Grigore, D., Lazăr, I., & Gheucă, I. (2015). New Middle and Upper Jurassic fossiliferous deposits mapped in the Rucăr area-Purcăreţului Valley (South Carpathians-Romania). In I. Bucur, I. Lazăr, & E. Săsăran (Eds.), *Tenth Romanian Symposium on Paleontology*, *Abstracts and Field TripGuide*. Cluj-Napoca, Romania: Cluj University Press.

Haas, J., Kovács, S., Gawlick, H.-J., Grădinaru, E., Karamata, S., Sudar, M., … Buser, S. (2011). Jurassic evolution of the tectonostratigraphic units of the Circum-Pannonian Region. *Jahrbuch Der Geologischen Bundesanstalt*, *151*(3–4), 281–354.

Hansel, C. M., Benner, S. G., Neiss, J., Dohnalkova, A., Kukkadapu, R., & Fendorf, S. (2003). Secondary mineralization pathways induced by dissimilatory iron reduction of ferrihydrite under advective flow. *Geochimica Et Cosmochimica Acta*, *67*, 2977–2992. https://doi.org/10.1016/S0016-7037(03)00276-X

Heimann, A., Johnson, C. M., Beard, B. L., Valley, J. W., Roden, E. E., Spicuzza, M. J., & Beukes, N. J. (2010). Fe, C, and O isotope compositions of banded iron formation carbonates demonstrate a major role for dissimilatory iron reduction in ~2.5 Ga marine environments. *Earth and Planetary Science Letters*, *294*, 8–18. https://doi.org/10.1016/j.epsl.2010.02.015

Heiri, O., Lotter, A. F., & Lemcke, G. (2001). Loss on ignition as a method for estimating organic and carbonate content in sediments: Reproducibility and comparability of results. *Journal of Paleolimnology*, *25*, 101–110.

Isley, A. E. (1995). Hydrothermal plumes and the delivery of iron to banded iron formation. *The Journal of Geology*, *103*(2), 169–185. https://doi.org/10.1086/629734

Jenkyns, H. C. (1971). The genesis of condensed sequences in the Tethyan Jurassic. *Lethaia*, *4*, p. 327–352. .https://doi.org/10.1111/j.1502-3931.1971.tb01928.x

Johnson, C. M., Beard, B. L., Klein, C., Beukes, N. J., & Roden, E. E. (2008). Iron isotopes constrain biologic and abiologic processes in banded iron formation genesis. *Geochimica Et Cosmochimica Acta*, *72*, 151–169. https://doi.org/10.1016/j.gca.2007.10.013

Kamber, B. S., Bolhar, R., & Webb, G. E. (2004). Geochemistry of late Archaean stromatolites from Zimbabwe; evidence for microbial life in restricted epicontinental seas. *Precambrian Research*, *132*, 379–399. https://doi.org/10.1016/j.precamres.2004.03.006

Kamber, B. S., & Webb, G. E. (2001). The geochemistry of late Archaean microbial carbonate: Implications for ocean chemistry and continental erosion history. *Geochimica Et Cosmochimica Acta*, *65*, 2509–2525. https://doi.org/10.1016/S0016-7037(01)00613-5

Kazmierczak, J., & Kempe, S. (2006). Genuine modern analogues of Precambrian stromatolites from caldera lakes of Niuafo'ou, Tonga. *Naturwissenschaften*, *93*, 119–126.

Konhauser, K. O., Hamade, T., Raiswell, R., Morris, R. C., Ferris, F. G., Southam, G., & Canfield, D. E. (2002). Could bacteria have formed the Precambrian banded iron formations? *Geology*, *30*(12), 1079–1082. https://doi.org/10.1130/0091-7613(2002)030<1079:CBHFTP>2.0.CO;2

Konhauser, K. O., Kappler, A., & Roden, E. E. (2011). Iron in microbial metabolisms. *Elements*, *7*, 89–93. https://doi.org/10.2113/gselements.7.2.89

Krepski, S. T., Emerson, D., Hredzak-Showalter, P. L., Luther, G. W., & Chan, C. S. (2013). Morphology of biogenic iron oxides records microbial physiology and environmental conditions: Toward interpreting iron microfossils. *Geobiology*, *11*, 457–471. https://doi.org/10.1111/gbi.12043

Lazăr, I. (2006). *Jurasicul mediu din Bucegi-versantul vestic-Paleontologie şi paleoecologie*. Bucureşti: Ars Docendi.

Lazăr, I., & Grădinaru, M. (2014). Paleoenvironmental context and paleoecological significance of unique agglutinated polychaete worm tube ferruginous microstromatolite assemblages from the Middle Jurassic of the Southern Carpathians (Romania). *Facies*, *60*, 515–540. https://doi.org/10.1007/s10347-013-0390-0

Lazăr, I., Grădinaru, M., & Petrescu, L. (2013). Ferruginous microstromatolites related to Middle Jurassic condensed sequences and hardgrounds (Bucegi Mountains, Southern Carpathians, Romania). *Facies*, *59*, 359–390. https://doi.org/10.1007/s10347-012-0313-5

Lin, Y., Tang, D., Shi, X., Zhou, X., & Huang, K. (2019). Shallow-marine ironstones formed by microaerophilic iron-oxidizing bacteria in

terminal Paleoproterozoic. *Gondwana Research*, *76*, 1–18. https://doi.org/10.1016/j.gr.2019.06.004

Lovely, D. R., Stolz, J. F., Nord, G. L., & Phillips, E. J. P. (1987). Anaerobic production of magnetite dissimilatory iron-reducing microorganism. *Nature*, *330*, 252–254.

Mamet, B., & Préat, A. (2003). Sur l'origine de la pigmentation de l'*Ammonitico Rosso* (Jurassique, région de Vérone, Italie du Nord). *Revue De Micropaléontologie*, *46*, 35–46.

Mamet, B., Préat, A., & DeRidder, C. (1997). Bacterial origin of the red pigmentation in the Devonian Slivenec Limestone, Czech Republic. *Facies*, *36*, 173–187. https://doi.org/10.1007/BF02536883

Mann, H., Tazaki, K., Fyfe, W. S., & Kerrich, R. (1992). Microbial accumulation of iron and manganese in different aquatic environments: An electron optical study. In H. C. W. Skinner, & R. W. Fitzpatrick (Eds.), *Biominrealization: Processes of iron and manganese* (pp. 115–132). Cremlingen, Germany: Catena Verlag.

Marshall, J. D., & Ashton, M. (1980). Isotopic and trace element evidence for submarine lithification of hardgrounds in the Jurassic of eastern England. *Sedimentology*, *27*, 271–289. https://doi.org/10.1111/j.1365-3091.1980.tb01178.x

McLennan, S. M. (1989). Rare earth elements in sedimentary rocks: Influence of provenance and sedimentary processes. *Review of Mineralogy*, *21*, 169–200.

Molina, J. M., & Reolid, M. (2010). Costras ferromanganesíferas pelágicas inducidas por comunidades bentónicas microbianas en el límite Jurásico Medio-Superior (Subbético Externo, provincia de Córdoba). *Geogaceta*, *48*, 59–62.

Năstăseanu, S. (1979). Geologie des Monts Cerna. *Anuarul Institutului De Geologie Si Geofizică*, *54*, 155–280.

Năstăseanu, S., Bercia, I., Iancu, V., Vlad, S., & Hârtopanu, I. (1981). The structure of the South Carpathians (Mehedinți – Banat Area). Carpatho-Balkan Geological Association, Twelve Congress, Guide to excursion B2, Bucharest, Guidebook Series 22, 100 pp

Neagu, T., Manea, I., & Gavrilescu, N. (1983). Studiul microbiostratigrafic al Doggerului din versantul vestic al Masivului Bucegi-Pasul Strunguliţa. *Ocrotirea naturii și mediului înconjurător*, *University of Bucharest Press*, *27*, 122–127.

Nozaki, Y., Zhang, J., & Amakawa, H. (1997). The fractionation between Y and Ho in the marine environment. *Earth and Planetary Science Letters*, *148*, 329–340. https://doi.org/10.1016/S0012-821X(97)00034-4

Ostrum, M. E. (1961). Separation of clay minerals from carbonate rocks by using acid. *Journal of Sedimentary Research*, *31*, 123–129.

Palmer, T. J., & Wilson, M. A. (1990). Growth of ferruginous oncoliths in the Bajocian (Middle Jurassic) of Europe. *Terra Nova*, *2*, 142–147. https://doi.org/10.1111/j.1365-3121.1990.tb00055.x

Patrulius, D. (1969) *Geologia Masivului Bucegi şi a Culoarului Dîmbovicioara*. Bucureşti: Editura Academiei Republicii Socialiste Romania.

Patrulius, D., & Popa, E. (1971). Lower and Middle Jurassic ammonite zones in the Roumanian Carpathians. *Annales Instituti Geologici Publici Hungarici*, *54*, 131–147.

Patrulius, D., Popa, E., Avram, E., Baltreş, A., Pop, G., Iva, M., … Iordan, M. (1980). Studiul petrologic şi biostratigrafic complex al formaţiunilor jurasice şi neocomiene din Carpaţii Româneşti şi Dobrogea în vederea evaluării potenţialului de resurse minerale. Sectorul Leaota-Braşov-Munţii Perşani. Raport IGG, Tema Nr. 47/1979.

Planavsky, N., Bekker, A., Rouxel, O. J., Kamber, B., Hofmann, A., Knudsen, A., & Lyons, T. W. (2010). Rare Earth Element and yttrium compositions of Archean and Paleoproterozoic Fe formations revisited: New perspectives on the significance and mechanisms of deposition. *Geochimica Et Cosmochimica Acta*, *74*, 6387–6405. https://doi.org/10.1016/j.gca.2010.07.021

Planavsky, N. J., Rouxel, O. J., Bekker, A., Hofmann, A., Little, C. T. S., & Lyons, T. W. (2012). Iron isotope composition of some Archean and Proterozoic iron formations. *Geochimica Et Cosmochimica Acta*, *80*, 158–159. https://doi.org/10.1016/j.gca.2011.12.001

Planavsky, N., Rouxel, O., Bekker, A., Shapiro, R., Fralick, P., & Knudsen, A. (2009). Iron-oxidizing microbial ecosystems thrived in late Paleoproterozoic redox-stratified oceans. *Earth and Planetary Science Letters*, *286*, 230–242. https://doi.org/10.1016/j.epsl.2009.06.033

Popa, E., Năstăseanu, S., & Antonescu, E. (1977). Nouvelles données concernant la biotratigraphie du Jurassique inférieur de la zone Sirinia (Banat). *Dări De Seamă, Institutl De Geologie Și Geofizică*, *63*, 7–24.

Popa, E., & Patrulius, D. (1996). Lower Jurassic ammonites in the Romanian Carpathians. *Memoriile Institutului Geologic Al României*, *36*, 53–63.

Préat, A. R., de Jong, J. T. M., Mamet, B. L., & Mattielli, N. (2008). Stable iron isotopes and microbial mediation in red pigmentation of the Rosso Ammonitico (Mid-Late Jurassic, Verona Area, Italy). *Astrobiology*, *8*, 1–17. https://doi.org/10.1089/ast.2006.0035

Préat, A., Mamet, B., Bernard, A., & Gillan, D. (1999). Bacterial mediation, red matrices diagenesis, Devonian, Montagne Noire (southern France). *Sedimentary Geology*, *126*, 223–242. https://doi.org/10.1016/S0037-0738(99)00042-1

Préat, A., Mamet, B., De Ridder, C., Boulvain, F., & Gillan, D. (2000). Iron bacterial and fungal mats, Bajocian stratotype (Mid-Jurassic, northern Normandy, France). *Sedimentary Geology*, *137*, 107–126. https://doi.org/10.1016/S0037-0738(00)00101-9

Préat, A., Mamet, B., Di Stefano, P., Martire, L., & Kolo, K. (2011). Microbially-induced Fe and Mn oxides in condensed pelagic sediments (Middle-Upper Jurassic, Western Sicily). *Sedimentary Geology*, *237*, 179–188. https://doi.org/10.1016/j.sedgeo.2011.03.001

Préat, A., Morano, S., Loreau, J. L., Durlet, C., & Mamet, B. (2006). Petrography and biosedimentology of the Rosso Ammonitico Veronese (middle-upper Jurassic, north eastern Italy). *Facies*, *52*, 265–278. https://doi.org/10.1007/s10347-005-0032-2

Răileanu, G. (1953). Cercetări geologice în regiunea Svinița-Fața Mare. *Buletin Stiințific al Academiei RPR*, *5*(2), 307–409.

Răileanu, G. (1960). Recherches geologiques dans la region Sviniţa - Faţa Mare. *Anuarul Comitetului de Stat al Geologiei România*, *26*(28), 347–383.

Reolid, M., & Abad, I. (2018). The Middle Upper Jurassic unconformity in the South Iberian Palaeomargin (Western Tethys): A history of carbonate platform fragmentation, emersion and subsequent drowning. *Journal of Iberian Geology*, *44*, https://doi.org/10.1007/s41513-018-0085-z

Reolid, M., Abad, I., & Martín-García, J. M. (2008). Palaeoenvironmental implications of ferruginous deposits related to a Middle-Upper Jurassic discontinuity (Prebetic Zone, Betic Cordillera, Southern Spain). *Sedimentary Geology*, *203*, 1–16. https://doi.org/10.1016/j.sedgeo.2007.10.001

Reolid, M., & Molina, J. M. (2010). Serpulid-Frutexites assemblage from shadow-cryptic environments in Jurassic marine caves, Betic Cordillera, southern Spain. *Palaios*, *25*, 468–474. https://doi.org/10.2110/palo.2009.p09-150r

Reolid, M., & Nieto, L. M. (2010). Jurassic Fe–Mn macro-oncoids from pelagic swells of the External Subbetic (Spain): Evidences of microbial origin. *Geologica Acta*, *8*, 151–168. https://doi.org/10.1344/105.000001525

Rosel, P., Oliveros, V., Ducea, M. N., Charrier, R., Scaillet, S., Retamala, L., & Figueroa, O. (2013). The Early Andean subduction system as an analogue to island arcs: Evidence from across-arc geochemical variations in northern Chile. *Lithos*, *179*, 211–230.

Rouxel, O., Bekker, A., & Edwards, K. (2005). Iron isotope constraints on the Archean and Paleoproterozoic Ocean redox state. *Science*, *307*, 1088–1091. https://doi.org/10.1126/science.1105692

Rouxel, O., Shanks, W. C., Bach, W., & Edwards, K. (2008). Integrated Fe and S isotope study of seafloor hydrothermal vents at East Pacific Rise 9–10 N. *Chemical Geology*, *252*, 214–227. https://doi.org/10.1016/j.chemgeo.2008.03.009

Rouxel, O., Toner, B., Germain, Y., & Glazer, B. (2018). Geochemical and iron isotopic insights into hydrothermal iron oxyhydroxide deposit formation at loihi seamount. *Geochimica Et Cosmochimica Acta*, *220*, 449–482. https://doi.org/10.1016/j.gca.2017.09.050

Salama, W., El Aref, M. M., & Gaupp, R. (2013). Mineral evolution and processes of ferruginous microbialite accretion - an example from the Middle Eocene stromatolitic and ooidal ironstones of the Bahariya Depression, Western Desert, Egypt. *Geobiology*, *11*, 15–28. https://doi.org/10.1111/gbi.12011

Sandoval, J., Checa, A. et al (2002). Taphonomy of cephalopod concentrations in the Jurassic of the Subbetic (Southern Spain). In M. De Renzi (Ed.), *Current topics on taphonomy and fossilization* (pp. 223–230). Ayuntamiento de Valencia: Valencia.

Săndulescu, M. (1984). *Geotectonica României*. Bucureşti: Editura Tehnică.

Săndulescu, M. (1994). Overview on Romanian geology. *Romanian Journal of Tectonics and Regional Geology*, *75*, 3–15.

Schwertmann, U., & Murad, E. (1983). Effect of pH on the formation of goethite and hematite from ferrihydrite. *Clays and Clay Minerals*, *31*, 277–284. https://doi.org/10.1346/CCMN.1983.0310405

Severmann, S., Johnson, C. M., Beard, B. L., German, C. R., Edmonds, H. N., Chiba, H., & Green, D. R. H. (2004). The effect of plume processes on the Fe isotope composition of hydrothermally derived Fe in the deep ocean as inferred from the Rainbow vent site, Mid-Atlantic Ridge, 36 degrees 14' N. *Earth and Planetary Science Letters*, *225*, 63–76.

Severmann, S., Johnson, C. M., Beard, B. L., & McManus, J. (2006). The effect of early diagenesis on the Fe isotope compositions of porewaters and authigenic minerals in continental margin sediments. *Geochimica Et Cosmochimica, Acta*, *70*, 2006–2022. https://doi.org/10.1016/j.gca.2006.01.007

Shapiro, R. S., & Konhauser, K. O. (2015). Hematite-coated microfossils: Primary ecological fingerprint or taphonomic oddity of the Paleoproterozoic? *Geobiology*, *13*, 209–224. https://doi.org/10.1111/gbi.12127

Sholkovitz, E. R., & Schneider, D. L. (1991). Cerium redox cycles and rare earth elements in the Sargasso Sea. *Geochimica Et Cosmochima Acta*, *55*, 2737–2743. https://doi.org/10.1016/0016-7037(91)90440-G

Slack, J. F., Grenne, T., Bekker, A., Rouxel, O. J., & Lindberg, P. A. (2007). Suboxic deep seawater in the late Paleoproterozoic: Evidence from hematitic chert and Fe formation related to seafloor-hydrothermal sulfide deposits, central Arizona, USA. *Earth and Planetary Science Letters*, *255*, 243–256.

Taylor, S. R., & McLennan, S. M. (1985). *The continental crust: Its composition and evolution* (p. 312). Oxford, UK: Blackwell Scientific Publications.

Tostevin, R., Shields, G. A., Tarbuck, G. M., He, T., Clarkson, M. O., & Wood, R. A. (2016). Effective use of cerium anomalies as a redox proxy in carbonate-dominated marine settings. *Chemical Geology*, *438*, 146–162. https://doi.org/10.1016/j.chemgeo.2016.06.027

Tucker, M. E. (1981). *Sedimentary petrology: An introduction* (pp. 252). Oxford: Blackwell.

Veizer, J., Ala, D., Azmy, K., Bruckschen, P., Buhl, D., Bruhn, F., … Strauss, H. (1999). 87Sr/86Sr, δ13C and δ18O evolution of Phanerozoic seawater. *Chemical Geology*, *161*, 59–88. https://doi.org/10.1016/S0009-2541(99)00081-9

von Blanckenburg, F., Marnberti, M., Schoenberg, R., Kamber, B. S., & Webb, G. E. (2008). The iron isotope composition of microbial carbonate. *Chemical Geology*, *249*, 113–128. https://doi.org/10.1016/j.chemgeo.2007.12.001

Webb, G. E., & Kamber, B. S. (2000). Rare earth elements in Holocene reefal microbialites: A new shallow seawater proxy. *Geochimica Et Cosmochimica Acta*, *64*, 1557–1565. https://doi.org/10.1016/S0016-7037(99)00400-7

Welch, S. A., Beard, B. L., Johnson, C. M., & Braterman, P. S. (2003). Kinetic and equilibrium Fe isotope fractionation between aqueous Fe(II) and Fe(III). *Geochimica Et Cosmochima Acta*, *67*, 4231–4250. https://doi.org/10.1016/S0016-7037(03)00266-7

SUPPORTING INFORMATION

Additional supporting information may be found online in the Supporting Information section.

How to cite this article: Grădinaru M, Lazăr I, Ducea MN, Petrescu L. Microaerophilic Fe-oxidizing micro-organisms in Middle Jurassic ferruginous stromatolites and the paleoenvironmental context of their formation (Southern Carpathians, Romania). *Geobiology*. 2020;00:1–28. https://doi.org/10.1111/gbi.12376